

An absorption-selected survey of neutral gas in the Milky Way halo

New results based on a large sample of Ca II, Na I, and HI spectra towards QSOs*

N. Ben Bekhti¹, B. Winkel², P. Richter³, J. Kerp¹, U. Klein¹, and M. T. Murphy⁴

¹ Argelander-Institut für Astronomie, Universität Bonn, Auf dem Hügel 71, 53121 Bonn, Germany
e-mail: nbekhti@astro.uni-bonn.de

² Max-Planck-Institut für Radioastronomie, Auf dem Hügel 69, 53121 Bonn, Germany

³ Institut für Physik und Astronomie, Universität Potsdam, Haus 28, Karl-Liebknecht-Str. 24/25, 14476 Potsdam, Germany

⁴ Centre for Astrophysics & Supercomputing, Swinburne University of Technology, Hawthorn, 3122 Victoria, Australia

Received 18 December 2011 / Accepted 22 March 2012

ABSTRACT

Aims. We aim at analysing systematically the distribution and physical properties of neutral and mildly ionised gas in the Milky Way halo, based on a large absorption-selected data set.

Methods. Multi-wavelength studies were performed combining optical absorption line data of Ca II and Na I with follow-up HI 21-cm emission line observations along 408 sight lines towards low- and high-redshift QSOs. We made use of archival optical spectra obtained with UVES/VLT. HI data were extracted from the Effelsberg-Bonn HI survey and the Galactic All-Sky survey. For selected sight lines we obtained deeper follow-up observations using the Effelsberg 100-m telescope.

Results. Ca II (Na I) halo absorbers at intermediate and high radial velocities are present in 40–55% (20–35%) of the sightlines, depending on the column density threshold chosen. Many halo absorbers show multi-component absorption lines, indicating the presence of sub-structure. In 65% of the cases, absorption is associated with HI 21-cm emission. The Ca II (Na I) column density distribution function follows a power-law with a slope of $\beta \approx -2.2$ (-1.4).

Conclusions. Our absorption-selected survey confirms our previous results that the Milky Way halo is filled with a large number of neutral gas structures whose high column density tail represents the population of common HI high- and intermediate-velocity clouds seen in 21-cm observations. We find that Na I/Ca II column density ratios in the halo absorbers are typically smaller than those in the Milky Way disc, in the gas in the Magellanic Clouds, and in damped Lyman α systems. The small ratios (prominent in particular in high-velocity components) indicate a lower level of Ca depletion onto dust grains in Milky Way halo absorbers compared to gas in discs and inner regions of galaxies.

Key words. Galaxy: halo – ISM: structure

1. Introduction

High-resolution emission and absorption measurements in different wavelength regimes have demonstrated that spiral galaxies at low and high redshifts are surrounded by extended gaseous haloes (e.g., Savage & Massa 1987; Majewski 2004; Fraternali et al. 2007; Boomsma et al. 2008; Steidel et al. 2010; Bouché et al. 2012; Rudie et al. 2012, and references therein). Sensitive observations suggest that up to 30% of the neutral hydrogen of a spiral galaxy could be located in the halo (e.g., Fraternali et al. 2001; Oosterloo et al. 2007). The origin and nature of this extra-planar gas in the halo is still uncertain, because the halo is continuously fuelled with gas by different mechanisms that are connected with the on-going formation and evolution of galaxies (outflows, galaxy merging and gas accretion from the intergalactic medium (IGM), e.g. Shapiro & Field 1976; Fraternali et al. 2004; Kaufmann et al. 2006; Sancisi et al. 2008).

Understanding the nature of extra-planar gas in galaxy haloes is important to characterise the infall of gaseous material feeding star formation and the outflow of gas as part of galactic winds. Since haloes represent the interface region between

the dense galactic discs and the surrounding IGM the study of matter exchange between galaxies and their environment is an important aspect in our understanding of the IGM.

A particularly powerful method for studying the properties and nature of extra-planar gaseous structures in the haloes of galaxies is the analysis of absorption lines in the spectra of distant quasars (QSOs). This can best be done in the optical and ultraviolet, since most of the ion transitions of interest for QSO absorption spectroscopy are located in these wavelength regimes. For a recent review we refer to Richter (2006). QSO absorption spectroscopy provides information about the physical properties, kinematics, and spatial distribution of gas in galaxy haloes over a large range of column densities. The analysis of different ions like Mg II, C IV, O I, Si II, and C II (e.g., Charlton et al. 2000; Ding et al. 2003a; Masiero et al. 2005; Bouché et al. 2006; Richter et al. 2009) along sight lines that pass through the halo of the Milky Way and the inner and outer regions of other galaxies reveal different types of absorbers (e.g., discs absorbers, infalling and outflowing gas, tidal structures). All of these have a specific range of physical properties, such as the degree of ionisation and the metallicity.

The most prominent gaseous structures in the Milky Way halo are the intermediate- and high-velocity clouds (IVCs, HVCs; Muller et al. 1963), which show radial velocities that

* Full Table 1 is only available at the CDS via anonymous ftp to cdsarc.u-strasbg.fr (130.79.128.5) or via <http://cdsarc.u-strasbg.fr/viz-bin/qcat?J/A+A/542/A110>

are inconsistent with a simple model of a Galactic disc rotation. They possibly represent one group of local analogues of extra-planar gas features seen in the vicinity of other galaxies. IVCs and HVCs represent multi-phase structures that can contain regions of partly molecular gas (H_2 absorption, Richter et al. 2001a; Wakker 2006), cold and warm neutral gas seen in 21-cm emission (Brüns et al. 2005; Ben Bekhti et al. 2008), warm-ionised plasma as traced by $\text{H}\alpha$ emission (Putman et al. 2003; Hill et al. 2009) and UV absorption (Lu et al. 1994), and highly-ionised plasma seen in O VI absorption (Sembach et al. 2003; Fox et al. 2006) and in X-ray emission (Kerp et al. 1999; de Boer 2004, and references therein).

Distance estimates of IVCs and HVCs around the Milky Way (e.g., Sembach et al. 1991; van Woerden et al. 1999; Wakker 2001; Thom et al. 2006; Wakker et al. 2007, 2008) indicate that most IVCs are relatively nearby objects at distances of $d < 2$ kpc, while HVCs are more distant clouds, located in the halo of the Milky Way at $5 < d < 50$ kpc.

Metal abundances of several IVCs/HVCs have been determined by absorption-line measurements (see reviews by Wakker 2001; Richter 2006). Results show metallicities varying between ~ 0.1 and ~ 1.0 solar. This wide range of metallicities suggests that not all IVCs and HVCs share a common origin. The chemical composition of some IVCs/HVCs with nearly solar metallicities can be explained by the galactic fountain model. There are, however, IVCs and HVCs with metal abundances clearly below solar. The Magellanic Stream, for example, has abundances similar to that of the Small Magellanic Cloud (~ 0.3 solar). There are also HVCs with abundances less than 0.3 solar (e.g., Complex C, Wakker et al. 1999; Richter et al. 2001b), but still larger than one would expect for primordial gas. The conclusion is that the gas has already been processed, but at different levels depending on the origin.

In our previous paper (Ben Bekhti et al. 2008, BB08 hereafter) we systematically analysed Ca II absorption and HI emission data of gas in the Milky Way halo towards about 100 QSOs and we generated a first absorption-selected halo-cloud sample. We found that next to the massive IVC/HVC complexes, there exists a population of low-column density absorbers with HI column densities of $N_{\text{HI}} < 10^{19} \text{ cm}^{-2}$ (Richter et al. 2005, BB08) that are traced by optical Ca II absorption. We further showed that optical halo absorbers have a substantial area-filling factor of about 30% (see also Richter et al. 2011), suggesting that low-column density neutral gas clumps represent an important absorber population that is important for our understanding of the gas distribution in the Milky Way halo.

In this follow-up paper we extend our previous study of extra-planar gas structures in the Milky Way halo. We almost quadrupled the size of our sample to a total of 408 extragalactic sight lines through the halo. This large data set allows us to perform a more solid statistical study of the absorbing structures. Furthermore, we now have a sufficiently large data base to provide statistical analyses independently for IVCs and HVCs and, even more important, to incorporate Na I into our investigation. The sky distribution of the sight lines is very homogeneous (though the Galactic plane and the region $\delta > 30^\circ$ is not traced). This is an important point, since the MW halo is known to contain gaseous structures at large angular scales (i.e., the 21-cm IVC/HVC complexes), which could bias our statistics if the analysis was based on a small or very inhomogeneous sky coverage.

For all the positions where Ca II and/or Na I halo absorption is detected we searched for counterparts in HI 21-cm emission. We performed deep pointed observations using the 100-m telescope at Effelsberg for selected sightlines. For the remaining

lines of sight we make use of the new large-area HI 21-cm surveys GASS (Galactic All-Sky survey, McClure-Griffiths et al. 2009; Kalberla et al. 2010) and EBHIS (Effelsberg-Bonn HI survey, Winkel et al. 2010; Kerp et al. 2011). Compared to BB08, this leads to a substantially increased number of HI spectra available for follow-up analyses. The large-area surveys also provide the opportunity to search for HI structures in the direct vicinity of the absorption sight lines. The study of these as well as of follow-up HI aperture synthesis observations is under-way and will be presented in a subsequent paper.

In Sect. 2 of our paper we describe the data acquisition and reduction as well as the sample of extra-planar clouds. In Sect. 3 the results of the statistical analysis are presented along with a discussion of the various findings. Finally, Sect. 4 summarises our work.

2. Data and cloud catalogue

2.1. UVES data

For our large absorption-selected data set we made use of the publicly available ESO data archive¹. We use 408 optical spectra of low- and high-redshift QSOs that were observed between 1999 and 2004 with the Ultraviolet and Visual Echelle Spectrograph (UVES) at the ESO Very Large Telescope (VLT). A detailed description of the UVES instrument is given by Dekker et al. (2000). The raw data were reduced and normalised as part of the UVES Spectral Quasar Absorption Database (SQUAD; PI: Michael T. Murphy) using a modified version of the UVES pipeline. For a more detailed description of the reduction steps see BB08 and Richter et al. (2011).

The reduced data set provides spectra with a resolution of $R \approx 40\,000\text{--}60\,000$, corresponding to a spectral resolution of $\delta v \approx 6.6 \text{ km s}^{-1}$ (FWHM). The pixel separation, $\Delta v \approx 2.5 \text{ km s}^{-1}$, is small enough to ensure full Nyquist sampling.

The spectral features were analysed via Voigt-profile fitting using the FITLYMAN package in MIDAS (Fontana & Ballester 1995), which, among other parameters, delivers column densities and Doppler parameters (b -values). The latter are automatically de-convolved by FITLYMAN to account for the instrumental (spectral) response function. Therefore, b -values obtained from the fit are usually much smaller than the apparent width of the absorption lines in the spectra. As a consequence, in many cases the obtained b -values are much smaller than the instrumental resolution, i.e., the profiles are unresolved. Therefore, they should be treated with care – they provide only an estimate of the true Doppler widths under the assumption that the absorption is due to a *single component*.

We use the Ca II $\lambda 3935, 3967$ and Na I $\lambda 5892, 5898$ doublets which were fitted simultaneously with FITLYMAN. For the normalised spectra the signal-to-noise ratio (S/N), $S/N_p = 1/\text{rms}$, per pixel was computed using MIDAS. It is important to note that the S/N_p values vary significantly for the different spectra and are also dependent on the wavelength. In Fig. 1 we show the distribution calculated for the spectral ranges near the two Ca II ($\sim 4000 \text{ \AA}$) and Na I ($\sim 6000 \text{ \AA}$) lines. The median value for Ca II is 15.5, while for Na I we find a median of 23.4. Unfortunately, in several cases one (or rarely both) desired spectral ranges of the 408 available data sets were corrupted. In total, our sample includes 306 (345) spectra suited to search for Ca II (Na I) absorption in the Milky Way halo.

¹ <http://archive.eso.org/wdb/wdb/eso/uves/form>

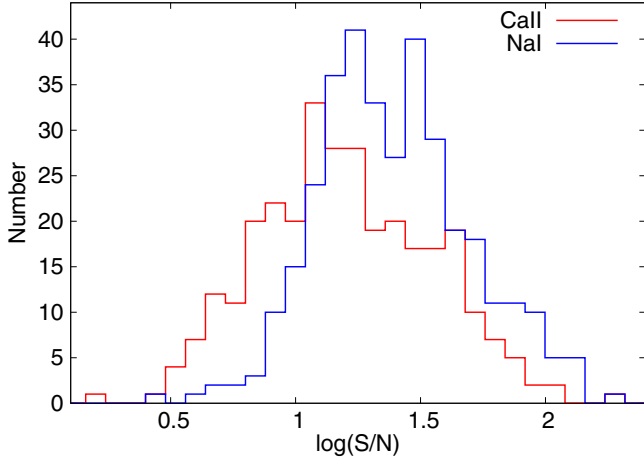


Fig. 1. Distribution of S/N_p values for the QSO absorption spectra in our sample.

2.1.1. Column density detection limits and sample completeness

From the S/N_p values we can compute a (theoretical) detection limit for Ca II and Na I for each spectrum. We consider a line as detected if the equivalent width, W_λ , of the stronger line of each doublet is at least six times the equivalent width limit, $W_\lambda^{\text{lim}}(1\sigma)$, for that spectrum.

The W_λ^{lim} values can be computed analytically if one makes the following simplifications. Firstly, for lower limits it is safe to assume that the absorption line profiles are Gaussian-like. Secondly, we use a typical expected line width of $w_{\text{CaII}} = 5.5 \text{ km s}^{-1}$ (FWHM, corresponding to a b -value of 3.3 km s^{-1}) and $w_{\text{NaI}} = 3.5 \text{ km s}^{-1}$ (FWHM, corresponding to a b -value of 2.1 km s^{-1})²; see also Sect. 3.3. These values have to be convolved with the instrumental resolution to obtain the “apparent” line width $\mathcal{D}v = \sqrt{w^2 + \delta v^2}$ in the spectra, i.e., $\mathcal{D}v_{\text{CaII}} \approx 8.6 \text{ km s}^{-1}$ and $\mathcal{D}v_{\text{NaI}} \approx 7.5 \text{ km s}^{-1}$, respectively.

After (hypothetical) smoothing of the spectra until the spectral resolution matches the apparent line widths a detection would be made in just one physical resolution unit (not pixel, as these are correlated due to the slight oversampling). Due to the smoothing the noise will decrease,

$$\text{rms}^{\text{sm}} = \text{rms} \sqrt{\frac{\delta v}{\mathcal{D}v}}. \quad (1)$$

Since, the lines are assumed to be Gaussian-shaped, one can easily calculate the integrated intensity,

$$W = I_0 \sqrt{2\pi} \frac{\mathcal{D}v}{\sqrt{8 \ln 2}}, \quad (2)$$

of a profile where I_0 is the amplitude of the Gaussian. To calculate the limit we set $I_0 = \text{rms}^{\text{sm}}$ and obtain

$$\begin{aligned} W_\lambda^{\text{lim}}(1\sigma) &= \text{rms} \sqrt{2\pi \frac{\mathcal{D}v}{\sqrt{8 \ln 2}} \frac{\delta v}{\sqrt{8 \ln 2}}} \quad [\text{km s}^{-1}] \\ &= \frac{\text{rms}}{\sqrt{8 \ln 2}} \frac{\lambda_0}{c} \sqrt{2\pi \mathcal{D}v \delta v} \quad [\text{\AA}]. \end{aligned} \quad (3)$$

This can be easily converted to a column density detection limit, via

$$N_{\text{limit}}(1\sigma) = \frac{W_\lambda m_e c^2}{\pi e^2 \lambda^2 f}, \quad (4)$$

² $w = 2 \sqrt{2 \ln 2} b \approx 1.66 b$.

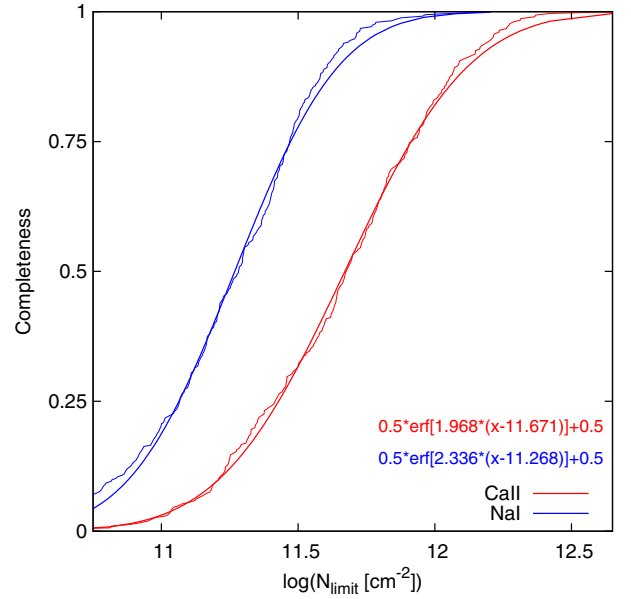


Fig. 2. Completeness, i.e., the ratio of the sight lines with a given detection limit compared to the total number of sight lines in the sample. To parametrise the curves for later use we fitted error functions to the data.

where f is the oscillator strength of the transition considered. Note, that the pixel resolution Δv does not enter the detection limits, but only the true (instrumental) resolution δv .

The column density limit values allow us to explore the completeness of the sample. In Fig. 2 we show the (cumulative) size of the Ca II and Na I samples if certain N_{limit} thresholds are applied. Both curves (thin solid lines) were normalised to unity and can be parametrised using an error function of the form

$$C(\log N_{\text{limit}}; a, b) = \frac{1}{2} \text{erf} [a(\log(N_{\text{limit}} - b))] + \frac{1}{2}. \quad (5)$$

This function C can be understood as a completeness function, as it returns the fraction of sight lines that can potentially reveal an absorber having a column density of $N \geq N_{\text{limit}}$. Note that the N_{limit} values are purely theoretical and likely need to be calibrated (i.e., shifting the parameter b) to match the true effective limits. However, the shape a of the true completeness function matches the values determined from Fig. 2.

2.2. EBHIS and GASS data

For our follow-up analysis we used data from the Effelsberg-Bonn H I Survey (EBHIS; Winkel et al. 2010; Kerp et al. 2011) and the Galactic All-Sky Survey (GASS; McClure-Griffiths et al. 2009; Kalberla et al. 2010), which are the most sensitive, highest angular resolution, large-scale surveys of Galactic HI emission ever made in the northern and southern sky. The former is currently undertaken with the 100-m telescope at Effelsberg, while the latter (using the 64-m Parkes telescope) was recently finished. Unfortunately, as the EBHIS is not yet completed for the full northern hemisphere, data was not available for every sight line.

The data reduction pipeline used for the GASS data is described in detail in Kalberla et al. (2010). The angular resolution of the final data cubes is $15'6$, leading to an rms level of 57 mK per spectral channel ($\Delta v = 0.8 \text{ km s}^{-1}$). For EBHIS the data reduction scheme presented in Winkel et al. (2010) was used. EBHIS has a slightly higher nominal noise level

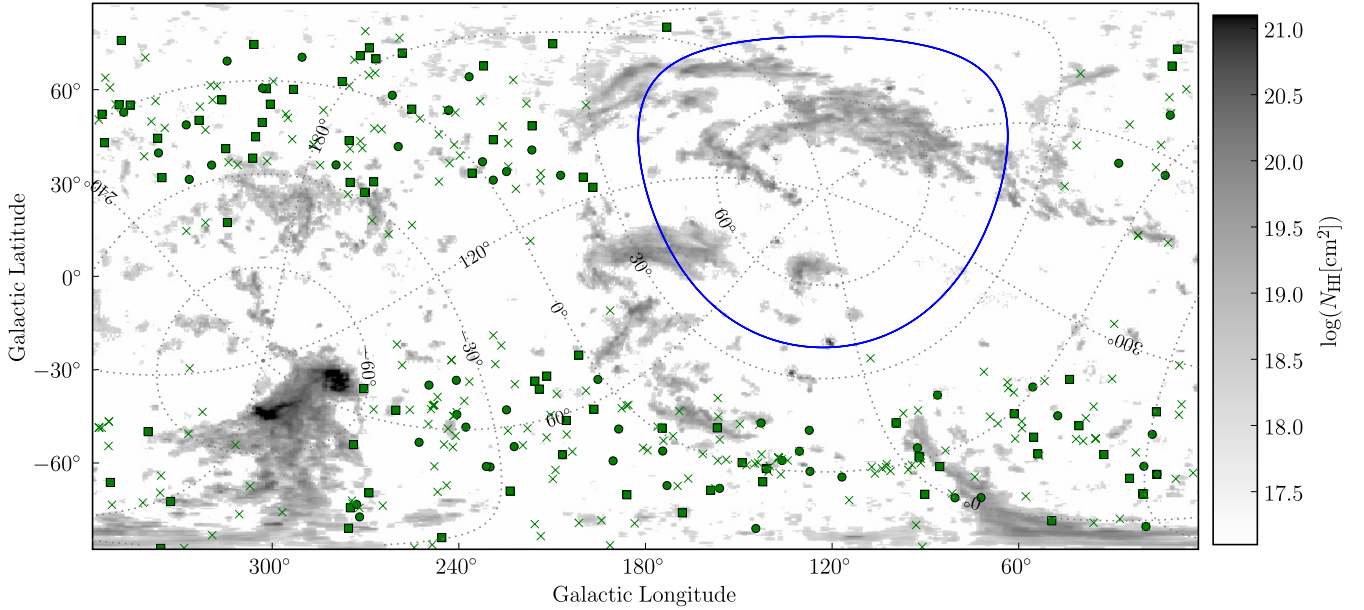


Fig. 3. HVC-all-sky map derived from the data of the LAB Survey (Kalberla et al. 2005) using a simple model of Galactic rotation kindly provided by Westmeier (for details see Westmeier 2007). The different symbols mark the locations of 408 QSO sight lines that were observed with UVES. Along 126 (75) lines of sight we detect Ca II (Na I) absorption components (marked with circles and boxes). The boxes mark the positions where we found corresponding H I emission. The crosses show non-detections. The blue line marks the region not accessible with the VLT ($\delta \geq 40^\circ$). Furthermore, the Galactic plane is not covered by our sample.

of $\lesssim 90$ mK ($\Delta v = 1.2$ km s $^{-1}$), but due to the better angular resolution of 10' the resulting column density detection limit (after angular smoothing to the Parkes beam) is almost identical: $N_{\text{HI}}^{\text{limit}} = 4.1 \times 10^{18}$ cm $^{-2}$ (GASS) and $N_{\text{HI}}^{\text{limit}} = 5.9 \times 10^{18}$ cm $^{-2}$ (EBHIS), calculated for a Gaussian-like emission line with a width of 20 km s $^{-1}$ (FWHM). All data sets were corrected for stray-radiation using the method of Kalberla et al. (1980) previously applied to the Leiden/Argentine/Bonn survey (LAB; Kalberla et al. 2005).

We also performed pointed observations towards 17 sources having $\delta > -30^\circ$ with the 100-m telescope at Effelsberg. The integration times for these pointed measurements were between 10 and 20 min, leading to an rms noise level of about 30...50 mK ($N_{\text{HI}}^{\text{limit}} = 2...4 \times 10^{18}$ cm $^{-2}$).

2.3. The sample

Figure 3 shows the population and distribution of high-velocity HI gas across the entire sky, based on the data of the LAB (grey scale). There are several coherent and extended HVC complexes covering the northern and southern sky, some of which are spanning tens of degrees like the Magellanic Stream, which is thought to have been stripped off the Magellanic Clouds by ram-pressure and/or tidal forces. New H I data obtained with EBHIS and GASS revealed that complexes like the Galactic center negative (GCN) are strongly fragmented into several warm and compact clumps (Winkel et al. 2011) if observed with higher resolution. Furthermore, numerous isolated and compact HVCs can be seen all over the sky (Braun & Burton 1999; Putman et al. 2002; de Heij et al. 2002).

The symbols in Fig. 3 mark the positions of the 408 sight lines that were observed with UVES (the blue line marks the region not accessible with the VLT). Along 126 lines of sight we detect 226 Ca II absorption components at intermediate or high velocities, as indicated by the filled circles and boxes. For Na I we found 96 components along 75 sight lines. H I spectra were

available for 133 lines of sight (EBHIS: 28, GASS: 88, pointed Effelsberg: 17). For 65% (EBHIS: 80%, GASS: 60%, pointed Effelsberg: 70%) of these we detect H I emission connected to the absorption features.

The conditional probability, $p(\text{Na I} | \text{Ca II})$, to find Na I if Ca II was detected is about 50%, while $p(\text{Ca II} | \text{Na I})$ is 90%, i.e. in just 6 of all cases we found only Na I but no Ca II along a sight line.

Figure 4 shows four example spectra of the sample with optical absorption of Ca II and Na I, along with the corresponding H I emission profiles observed with GASS and EBHIS, respectively. Most of the emission and absorption near zero velocities can be attributed to the local Galactic disc. To decide whether the gas in a given direction participates in Galactic disc rotation or not, we used a kinematic Milky Way model of the warm neutral medium (WNM, Kalberla 2003; Kalberla et al. 2007) and the concept of the deviation velocity, v_{dev} , that is the difference of the radial velocity and the terminal velocity of the Milky Way disc as introduced by Wakker (1991). The model of the WNM disc gas predicts for each line of sight the radial velocity, the density, and the so-called f -layer as a function of distance, (out to 50 kpc). The f -layer, f_z , is defined as

$$f_z = (z - z_{\text{disc}}) / w_{\text{disc}} \quad (6)$$

with z_{disc} the mean offset of the WNM from $z = 0$, i.e., z_{disc} describes the Milky Way warp, and w_{disc} the exponential scale height of the WNM. The latter accounts for the flaring of the disc. Its local value is 400 pc. For each line of sight we used the model to find the distance at which $f_z > 4$ and extracted the associated radial velocities. They should resemble rather conservative limits on typical velocities of the WNM. Of course local phenomena cannot be predicted by the model, so in few cases we might wrongly classify a cloud as being located in the halo when it is in fact disc material (and vice versa).

Supporting our previous results, 35% of the detected halo Ca II and 20% of Na I halo absorbers show multiple

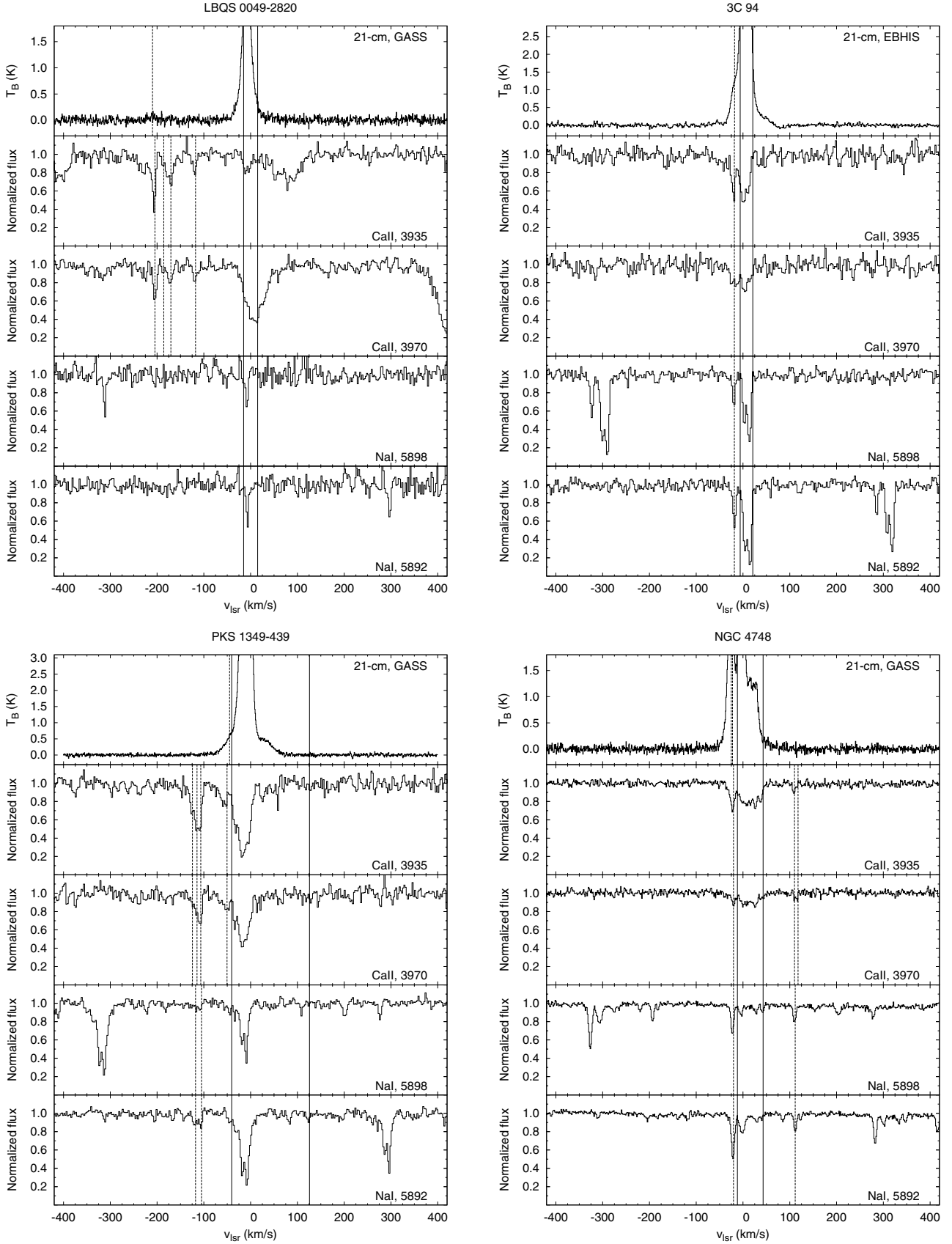


Fig. 4. Example Ca II and Na I absorption and H I emission spectra in the direction of the quasars LBQS 0049–2820, 3C 94, PKS 1349–439 and NGC 4748 obtained with UVES, EBHIS, and GASS. Detected components are indicated by dashed lines. The solid lines mark the v_{lsr} velocity range expected for Milky Way gas according to a model; see text.

intermediate- and high-velocity components, indicating the presence of sub-structure (see Sect. 3.10). Typical HI column densities of the gas structures lie in the range of $2 \times 10^{18} \text{ cm}^{-2}$ (detected in the pointed Effelsberg observations) up to $2 \times 10^{20} \text{ cm}^{-2}$. Typical HI line widths vary from $\Delta v_{\text{FWHM}} = 4 \text{ km s}^{-1}$ to 25 km s^{-1} , although the distribution is very wide-spread and several detections have more than 25 km s^{-1} , which can possibly be explained by substructure (compare Sect. 3.3). These values convert to upper kinetic temperature limits ranging from 100 K up to about 10^4 K , as expected for CNM and WNM, respectively. Measured column densities and b -values for all sight lines are summarised in Table 1.

The directions as well as the velocities of 45% (40%) of the halo Ca II (Na I) absorption components indicate a possible association with known HVC or IVC complexes (see Sect. 3.6). The other components, in contrast, do not appear to be associated with any known HVC or IVC complex. Confirming our previous results, optical absorption spectra allow us to trace the full column density range of neutral gas structures in the Galactic halo. The distribution of neutral or weakly ionised gas obviously is more complex than indicated by HI 21-cm observations alone.

Five sight lines (QSO B1448–232, HE 0001–2340, QSO B0450–1310B, [HB89] 1331+170 and HS 0810+2554) with prominent halo Ca II and Na I absorption lines were previously analysed with data from the Very Large Array (VLA) and the Westerbork Radio Synthesis Telescope (WSRT). The high-resolution HI data resolve the IVCs/HVCs into several compact, cold clumps (Richter et al. 2005; Ben Bekhti et al. 2009). Additional lines of sight have been re-observed in a similar manner and the results will be presented in a forthcoming paper.

3. Results of the statistical analysis

The large data sample allows us to perform a solid statistical analysis of the optical halo absorption components. In contrast to BB08 we are now able to include Na I into the analysis as well.

3.1. Column densities

Figure 5 shows a histogram of the *observed* column densities of the Ca II and Na I halo absorbers. The column densities range from $\log(N_{\text{CaII}}/\text{cm}^{-2}) = 10.5 \dots 13.5$ to $\log(N_{\text{NaI}}/\text{cm}^{-2}) = 10 \dots 13.3$. Interpretation of the numbers is very difficult, because our sample is very inhomogeneous in terms of sensitivity. The peak of the histogram at $\log(N)/\text{cm}^{-2} \sim 11.5$ is mainly due to selection effects.

Figure 6 shows the distribution of all HI column densities in our halo sample observed with Effelsberg, EBHIS and GASS (green line). The blue line displays the histogram of $\log N_{\text{HI}}$ for cases where both Ca II and Na I were also detected, while the red line is associated to those components where only Ca II was detected. The probability to find higher HI column densities (above $\log(N_{\text{HI}}/\text{cm}^{-2}) \gtrsim 19.8$) in our sample is slightly higher if both Ca II and Na I are present, and not only Ca II.

This can be seen more clearly in Fig. 7 which displays the number of sight lines with Ca II (upper panel) and Na I (lower panel) halo absorption with (red lines, A1) and without (blue lines, A2) corresponding HI emission. We find HI in almost all cases where Na I was previously detected. Apparently, with our HI and Na I data we are (detection-)limited to structures of similar gas column densities, while for Ca II the limiting column

density is about 0.5 dex lower. Hence, Ca II can be considered a much better probe to study the low-column density gas phase in the Galactic halo.

In Fig. 8 we show column density histograms separately for IVC and HVC gas. To decide whether a cloud is considered as high- or intermediate velocity we use the deviation velocity defined by Wakker (1991), which is the velocity distance to the closer terminal velocity of MW disc gas. Based on Wakker (1991) we classify absorbers with $|v_{\text{dev}}| \geq 50 \text{ km s}^{-1}$ as HVCs. While for Ca II about one third of the absorbers originates from high-velocity gas, only a tiny fraction of Na I detections stems from HVCs. The latter also have very low column densities, while the Ca II is similar for IVCs and HVCs; only the total number of absorbers is different.

3.1.1. Column density distribution functions

Figure 9 shows the Ca II and Na I column density distribution (CDD) functions,

$$f(N) = \frac{1}{M} \frac{m(N)}{\Delta N}, \quad M = \int_{N_{\text{min}}}^{N_{\text{max}}} f(N) dN \quad (7)$$

the normalised number of absorbers $m(N)$ per column density interval $[N, N + \Delta N]$ (Churchill et al. 2003, BB08).

Due to the increasing incompleteness of our sample the CDD drops off towards smaller column densities. While one usually circumvents this problem by using only the rightmost values for fitting the slope (e.g., BB08; Richter et al. 2011) we incorporate the inferred sample completeness function (see Sect. 2.1.1) into fitting of the CDD. This has two major advantages. First, one does not need to introduce an arbitrary threshold to the CDD values used for the fit and second, one can use all of the data points, thus increasing the statistical significance of the fit. In order to include the completeness into the fit, one just has to multiply the power-law fit function with the completeness function, $C(\log N; a, b)$. For convenience, we convert to the log–log regime where, instead of fitting a linear function to the rightmost data points (as in BB08), we use

$$f(\log N) = \beta \log N + n + \log C(\log N; a, b) \quad (8)$$

to parametrise the CDD. Here, β is the slope of the underlying power-law, n is a normalisation constant. In Fig. 9 the result of a χ^2 -fit is shown. Note that only the offset b of the completeness function was fitted, while the shape parameter a was kept constant (i.e., $a_{\text{CaII}} = 1.968 \text{ cm}^2$, $a_{\text{NaI}} = 2.336 \text{ cm}^2$), the values of which were determined in Sect. 2.1.1. The resulting offset values of $b_{\text{CaII}} = 11.8 \text{ cm}^{-2}$, $b_{\text{NaI}} = 11.2 \text{ cm}^{-2}$ are not completely matching the theoretical predictions, but are similar. The difference could be explained with blending of lines, an effect which decreases the completeness of our sample, but has not been incorporated into the S/N_p -statistics. Furthermore, the detected lines have of course different line widths, while for the detection limits a constant width was assumed for all spectra.

We obtain power-law slopes of $\beta_{\text{CaII}} = -2.2 \pm 0.2$ and $\beta_{\text{NaI}} = -1.4 \pm 0.1$. The former is steeper than found in BB08, but still consistent within 3σ confidence with the older result. However, the new finding has smaller errors and describes the CDD much better (in terms of reduced χ^2).

Our Ca II slope is also steeper than found for extra-galactic samples (e.g., Richter et al. 2011, $\beta_{\text{CaII}} \approx -1.7$), which is, however, not too surprising. In the latter not only pure halo absorbers are measured but also discs (having HI column densities of up

Table 1. QSO sight lines along which halo Ca II and Na I was detected. For many of them, a follow-up search for H I emission was performed.

QSO	RA [hhmmss.s]	Dec [ddmmss]	l [deg]	b [deg]	v_{lsr} [km s ⁻¹]	$\log N_{\text{Ca II}}$ [cm ⁻²]	$b_{\text{Ca II}}$ [km s ⁻¹]	$\log N_{\text{Na I}}$ [cm ⁻²]	$b_{\text{Na I}}$ [km s ⁻¹]	$\log N_{\text{H I}}$ [cm ⁻²]	$b_{\text{H I}}$ [km s ⁻¹]	Complex
HE 0001-2340	00 03 45.0	-23 23 55	49.39	-78.60	-126	11.89	6.0	-	-	-	-	MS
QSO B0002-422 (<i>HB89/0002-422</i>)	00 04 48.2	-41 57 28	332.68	-72.37	89	11.75	5.7	-	-	19.95	18.8	MS
SDSS J000815.33-095854.0	00 08 15.3	-09 58 54	90.19	-70.06	-202	11.62	6.0	-	-	-	-	MS
2QZ J000852.7-290044	00 08 52.7	-29 00 44	19.11	-80.43	-48	11.55	6.0	-	-	18.72	8.1	MS
FBQS 10040-0146	00 40 57.6	-01 46 32	116.84	-64.52	-36	12.53	7.0	-	-	-	-	MS
LBQS 0042-2930	00 45 08.5	-29 14 32	335.84	-87.47	-177	12.02	4.1	-	-	-	-	MS
LBQS 0049-2820	00 51 27.2	-28 04 35	302.73	-89.05	-28	12.23	3.4	11.63	2.0	18.69	14.8	MS
LBQS 0056-0009	00 59 05.5	+00 06 52	127.11	-62.70	-118	11.61	3.2	-	-	-	-	MS
QSO J0103+1316 (<i>HB89/0100+130</i>)	01 03 11.3	+13 16 18	127.34	-49.50	-171	11.97	8.0	-	-	-	-	MS
UM 669	01 05 16.8	-18 46 42	144.52	-81.06	-186	11.24	1.1	-	-	-	-	MS
UM 086	01 08 21.8	+06 23 28	130.51	-56.23	-205	12.15	3.0	-	-	18.14	6.1	MS
QSO B0109-353 (<i>HB89/0109-353</i>)	01 11 43.6	-35 03 01	275.47	-80.97	17	11.99	1.1	n/a	n/a	-	-	MS
QSO B0112-30 (<i>VCV96/0112-30</i>)	01 15 04.7	-30 25 14	246.77	-83.86	-351	11.72	4.0	10.98	3.0	-	-	MS
3C 37	01 18 18.5	+02 58 06	136.12	-59.21	106	11.43	2.0	-	-	-	-	MS
PKS 0119-04	01 22 27.9	-04 21 27	142.30	-66.06	167	11.24	3.2	-	-	-	-	MS
QSO B0122-379 (<i>HB89/0122-379</i>)	01 24 17.4	-37 44 23	271.91	-77.34	192	11.36	1.0	-	-	-	-	MS
FBQS J0125-0018	01 25 17.2	-00 18 29	141.18	-61.97	-26	11.43	4.4	n/a	n/a	n/a	n/a	MS
FBQS J0125-0005	01 25 28.8	-00 05 56	141.16	-61.76	-108	12.44	7.0	-	-	19.17	22.3	MS
2MASS J0129449-403345	01 29 44.9	-40 33 45	274.88	-74.41	79	12.41	6.9	11.03	6.0	-	-	MS
PKS 0130-17	01 32 43.5	-16 54 49	168.12	-76.02	-162	12.28	12.6	-	-	19.54	13.9	MS
[ICS96]013312.9-412216	01 35 23.2	-41 06 57	272.86	-73.35	-5	11.89	2.0	-	-	19.24	3.6	MS
SDSS J013901.40-082443.9	01 39 01.4	-08 24 44	156.17	-68.16	-13	11.89	2.0	13.07	0.5	20.10	15.3	MS
					-17	12.09	4.5	12.68	2.1	n/a	n/a	MS
					-48	11.59	1.6	-	-	19.74	14.1	MS
					40	11.72	3.9	-	-	-	-	MS
					-302	12.90	19.5	-	-	-	-	MS
					-54	11.43	0.8	11.29	0.6	19.52	16.9	MS
					-33	11.54	4.8	-	-	-	-	MS
					8	11.82	7.0	11.11	0.7	20.12	13.4	MS
					285	13.14	0.7	-	-	-	-	MS
					-100	12.18	2.0	-	-	-	-	MS

Notes. The table contains galactic coordinates, l and b , radial velocity, v_{lsr} , column densities, and $\log N$, b -values of all identified components. If an association to a known IVC/HVC complex is likely, the name of the complex is given in the last column. Primary QSO names are according to the SIMBAD database (<http://simbad.u-strasbg.fr/simbad/>). In some cases the SIMBAD identifiers cannot be found in the NASA/IPAC extragalactic database (NED, <http://ned.ipac.caltech.edu/>). In these cases the NED identifier is given in parentheses. The full table is only available in electronic form at the CDS. The electronic version additionally contains rms noise values for each spectrum and errors on $\log N$ and b -values. n/a data not available – non-detection.

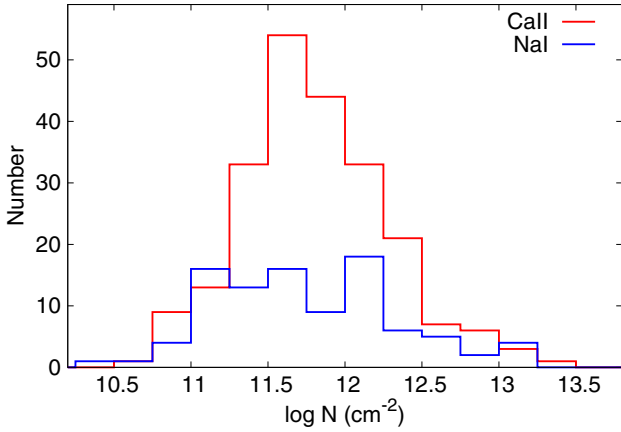


Fig. 5. Observed column density distributions of the Ca II and Na I absorbers.

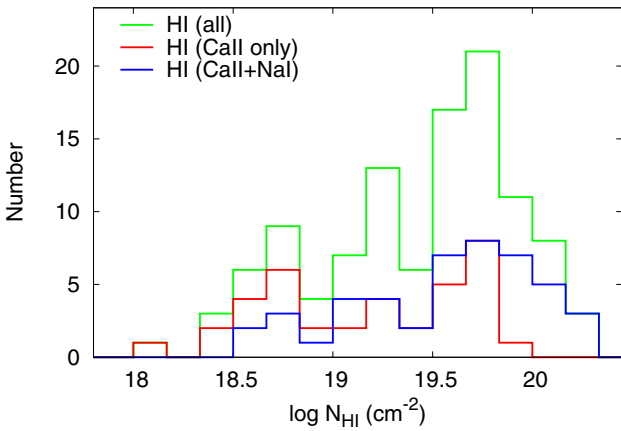


Fig. 6. Distribution of all H I column densities (green line). The blue line displays the number of absorbers where both, Ca II and Na I, is present, while the red line is for components showing only Ca II.

to 10^{22} cm^{-2}) which thus flattens the CDD. Another effect probably is the depletion of Calcium onto dust grains. As our absorber sample contains a good fraction of HVCs (which are known to have little dust), more Ca will reside in the free form in the high-velocity structures, which populate preferentially the low-column density regime. Especially the latter effect can be seen in Fig. 10 where we calculated the CDD separately for IVCs and HVCs. High-velocity gas shows even steeper CDD slopes (though the residual scatter is somewhat larger due to the smaller sample sizes), while the IVC slope is slightly flatter than that of the full sample. Dust depletion is further discussed in Sect. 3.7.

Using the correlations

$$\log(N_{\text{HI}}/\text{cm}^{-2}) = 4.55 \left[\log(N_{\text{CaII}}/\text{cm}^{-2}) - 7.45 \right] \quad (9)$$

$$\log(N_{\text{HI}}/\text{cm}^{-2}) = 1.19 \left[\log(N_{\text{NaI}}/\text{cm}^{-2}) + 5 \right], \quad (10)$$

between Ca II, Na I and HI found by Wakker & Mathis (2000), we can convert the Ca II and Na I column densities into HI column densities. One should keep in mind though that the conversion formula is affected by uncertainties as discussed in their paper.

Figure 11 shows the converted HI column density distribution functions $f(N)$ calculated from the Ca II and Na I column densities. The solid lines represent again the best-fit through the data using Eq. (8). Apparently, the slopes $\beta_{\text{HI}[\text{CaII}]} = -1.26 \pm 0.02$ and $\beta_{\text{HI}[\text{NaI}]} = -1.44 \pm 0.06$ inferred from the two species differ. Although both values are still consistent within a 3σ -level,

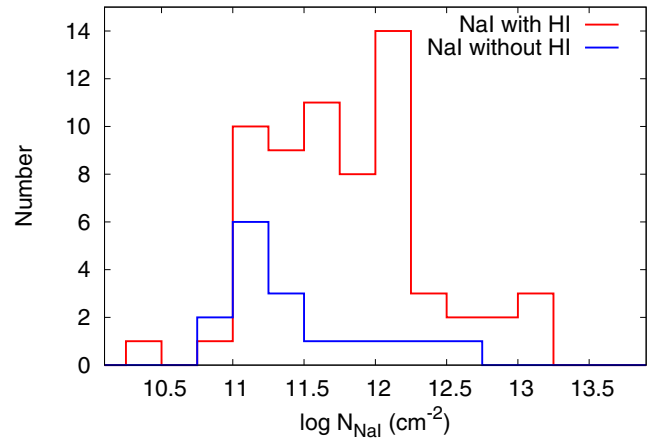
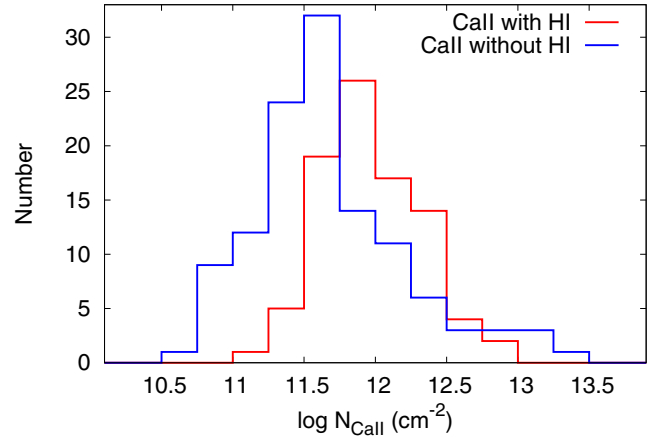


Fig. 7. Number of Ca II and Na I absorbers with (red lines) and without (blue lines) corresponding HI emission.

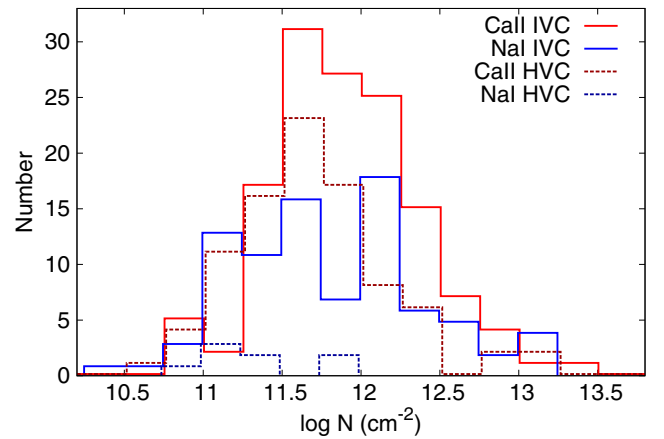


Fig. 8. Column densities of the absorbers separated by their deviation velocity. IVCs have $|v_{\text{dev}}| < 50 \text{ km s}^{-1}$, while HVCs have $|v_{\text{dev}}| \geq 50 \text{ km s}^{-1}$.

it is likely that the conversion formula of Wakker & Mathis (2000) is not perfectly in agreement with our halo-absorber data. Dust depletion might play a role, as in the halo we expect more Calcium to reside in the free form which would flatten the CDD (with respect to Na I) (compare Sect. 3.7). Furthermore, Wakker & Mathis (2000) used data having $\log(N_{\text{HI}}/\text{cm}^{-2}) \gtrsim 18$, which means that our Ca II CDD data points below this threshold are nothing else than extrapolation. Below $\log(N_{\text{HI}}/\text{cm}^{-2}) \sim 17$ the conversion formula even leads to unphysically high (i.e., above solar) abundance ratios.

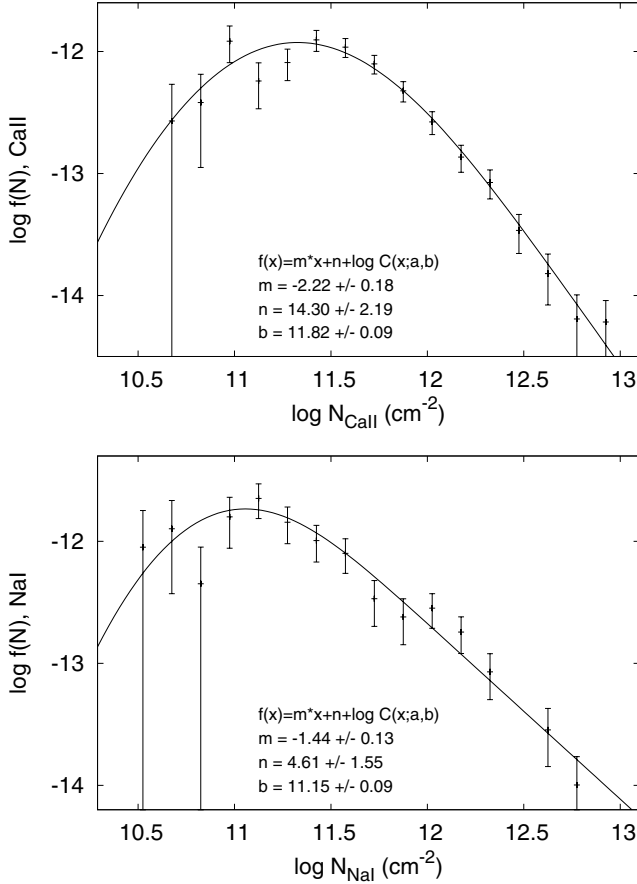


Fig. 9. The Ca II and Na I column density distributions $f(N)$ (using logarithmic binning). The solid lines represent a power-law fit under consideration of the completeness function of our sample. From χ^2 -fitting we obtain a slope of $\beta = -2.2 \pm 0.2$ for Ca II and $\beta = -1.4 \pm 0.1$ for Na I.

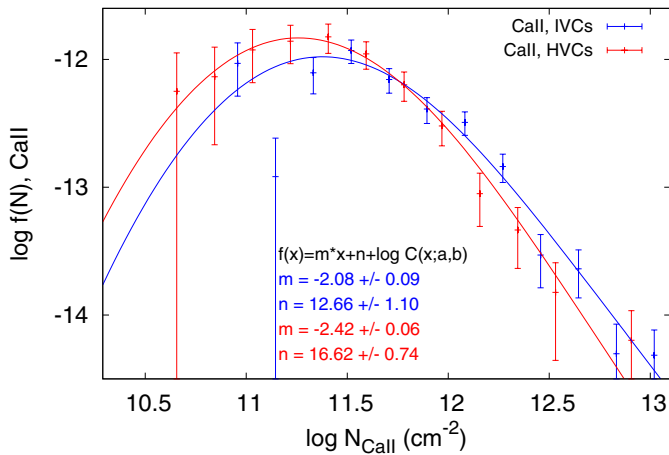


Fig. 10. The Ca II column density distributions $f(N)$ separately for IVC and HVC gas. Note that the completeness function $C(\log N; a, b)$ was kept fixed using the values from Fig. 9.

Again, we can compare the (converted) HI slope with the value of $\beta_{\text{HI}[\text{CaII}]} = -1.33 \pm 0.11$ found in BB08. Apparently, the results are consistent within 1σ , but the new finding has much lower error bars.

One can also compare the converted HI CDD with other samples. Petitjean et al. (1993) used low- and high-redshift ($\langle z \rangle = 2.8$) QSO absorption line data to obtain a slope

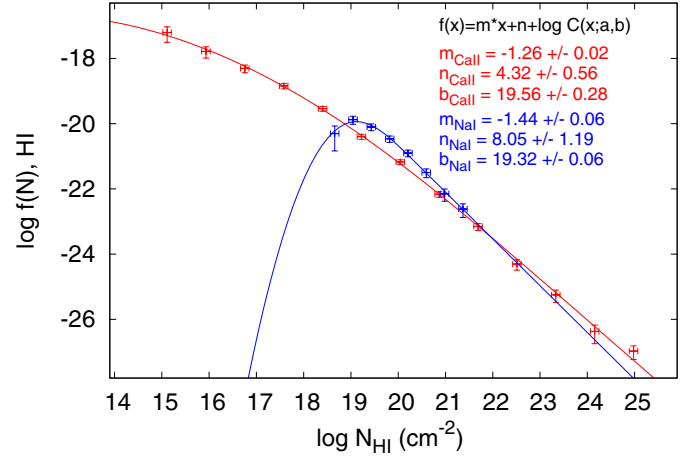


Fig. 11. Converted HI column density distribution functions $f(N)$. The HI column densities were calculated from the Ca II and Na I column densities using the correlation found by Wakker & Mathis (2000). The solid lines represent power-law fits (again corrected for completeness of the sample), with a slope of $\beta_{\text{HI}[\text{CaII}]} = -1.26 \pm 0.02$ and $\beta_{\text{HI}[\text{NaI}]} = -1.44 \pm 0.06$.

of $\beta_{\text{HI}} = -1.32$ for the $\log(N_{\text{HI}}/\text{cm}^{-2}) > 16$ regime. This is consistent with our values of $\beta_{\text{HI}[\text{CaII}]} = -1.26 \pm 0.02$ and $\beta_{\text{HI}[\text{NaI}]} = -1.44 \pm 0.06$, despite the issues with the conversion formula of Wakker & Mathis (2000) which does not account for dust-depletion effects.

Using 21-cm line emission data only, Lockman et al. (2002) find a distribution of $\beta_{\text{HI}} \sim -1$ which is not in agreement with our data. However, if beam-smearing plays a role (which is indicated by recent observations, e.g., Winkel et al. 2011), their column density detection limit of $\log(N_{\text{HI}}/\text{cm}^{-2}) \sim 17.9$ not only needs to be increased, but replaced with a certain selection function that could lead to a steeper CDD.

3.2. Deviation velocities

Figure 12 shows the deviation velocities, v_{dev} , of all observed Ca II and Na I halo absorbers versus galactic longitude (l) and latitude (b). We use v_{dev} to separate Milky-Way disc gas from intermediate- and high-velocity clouds. The size of the triangles in Fig. 12 is proportional to the logarithm of the Ca II and Na I column densities observed with UVES. For reference, the triangles in the legend have column densities of $N_{\text{CaII,NaI}} = 1 \times 10^{12} \text{ cm}^{-2}$. In these plots, there is no systematic trend visible in the velocity distributions.

Figure 13 shows a histogram of absorption components as a function of deviation velocity. The figure indicates that IVCs and HVCs trace different cloud populations, as the histograms cannot be described by a single (Gaussian-like) distribution, but rather by a narrow IVC population superposed onto a broad HVC distribution. In addition, we find an excess of negative deviation velocities. It is unlikely that this is due to a selection effect caused by the missing north-eastern part in our sample, as most of the known complexes in that area have negative deviation velocities (Wakker 1991). Such an excess was also reported by Blitz et al. (1999). They calculated the mean velocity and dispersion for different velocity rest frames. To compare our sample with the data of Blitz et al. (1999) we show in Table 2 the median velocity, $\langle v \rangle$, and velocity dispersion, $\langle v^2 \rangle$, of halo Ca II and Na II absorbers for various rest frames, separated for

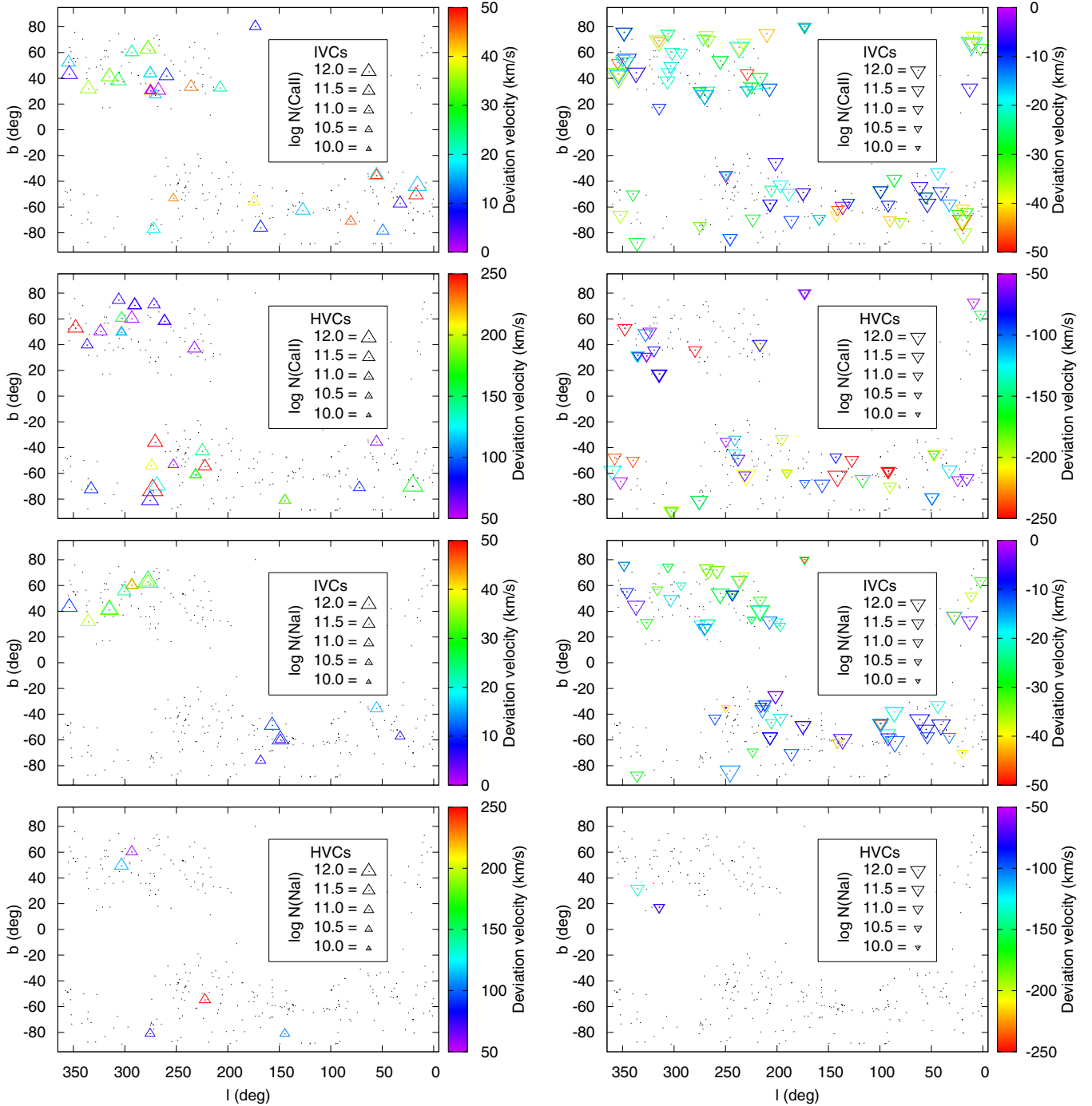


Fig. 12. Distribution of deviation velocities of the observed intermediate- and high-velocity Ca II and Na I absorbers versus Galactic longitude and latitude. The dimensions of the triangles are proportional to the logarithm of the Ca II and Na I column densities observed with the UVES instrument. The black dots mark the position of all sight lines for which spectra were available.

intermediate and high velocities. As only 6 Na II HVCs were detected we omit the latter.

The values in the tables are again subject to the inhomogeneous coverage of our sample and to some extent also to the different sensitivities of the sight lines. At least the latter effect should be not too large – the noise levels are distributed more or less randomly on the sky. This is mainly, because the sight lines in our sample were not observed to study the MW halo in the first place.

Not surprisingly, the dispersion of the IVC distributions is lowest in the LSR and deviation velocity frame. As for the full

sample, there is a negative-velocity excess. In contrast to the results of Blitz et al. (1999), the dispersion of HVCs in our sample is not smaller in the Local Group standard-of-rest frame (LGSR) and GSR. The LSR dispersion value is similar to that of Blitz et al. (1999) with $\sim 160 \text{ km s}^{-1}$. However, we cannot reproduce their much smaller GSR and LGSR dispersion values of $\sim 100 \text{ km s}^{-1}$.

Regardless of the rest frame we observe a mean velocity that is significantly below zero (about $-75 \dots -90 \text{ km s}^{-1}$ and -20 km s^{-1} for HVCs and IVCs, respectively). We attribute the excess of negative velocities to a net infall of gas onto the

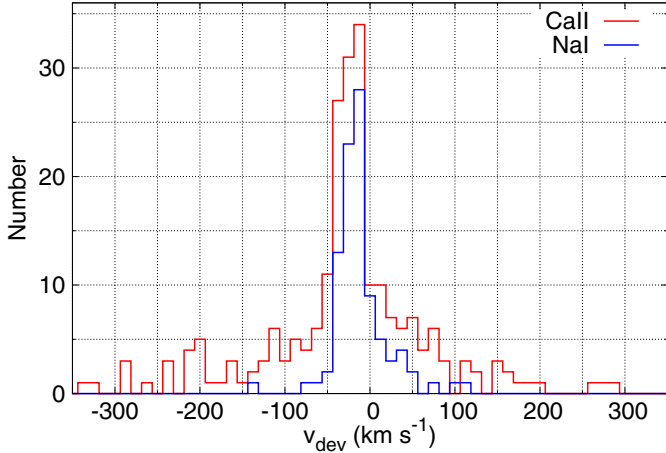


Fig. 13. Number of Ca II and Na I absorbers versus deviation velocity.

Table 2. Median velocities, $\langle v \rangle$, for different rest frames (deviation velocities, local, Galactic, and Local Group standard of rest) and velocity dispersions separated for intermediate- and high-velocity clouds.

Frame	IVC				HVC	
	Ca II $\langle v \rangle$	Ca II $\langle v^2 \rangle$	Na I $\langle v \rangle$	Na I $\langle v^2 \rangle$	Ca II $\langle v \rangle$	Ca II $\langle v^2 \rangle$
DEV	-17	24	-15	20	-74	150
LSR	-20	45	-18	22	-90	160
GSR	-42	90	-63	100	-92	150
LGRS	-66	120	-72	130	-90	170
Sample size	136		88		90	

Notes. All velocities are given in km s^{-1} .

Milky Way disc for both, IVCs and HVCs, which is in agreement with the findings of [Marasco & Fraternali \(2011\)](#) who used LAB data to find a best-fit model for extra-planar gas in the MW. They report on both, vertical ($v_z = -20 \text{ km s}^{-1}$) and radial ($v_R = -30 \text{ km s}^{-1}$), infall.

Note that we find 17 sight lines with very high deviation velocities of $|v_{\text{dev}}| > 200 \text{ km s}^{-1}$. Twelve of these pass the region between the anti-center complex and the Magellanic system, two pass HVC complex GCN, for both of which high negative deviation velocities are commonly observed. The remaining three sight lines (PKS 0922+14, HE 1126–2259, and QSO B1429–0053B) cannot be associated to a known HVC structure.

3.3. Doppler parameters and multi-component structure

Figure 14 shows the distribution of Doppler parameters (b -values) for our halo-absorber sample. The b -value distribution of Ca II peaks at $b = 1 \dots 2 \text{ km s}^{-1}$ and the maximum for Na I lies at $b = 2 \dots 3 \text{ km s}^{-1}$. In case of Ca II, a broad tail extends to $b \approx 13 \text{ km s}^{-1}$. The median values are $b_{\text{CaII}} = 3.3 \text{ km s}^{-1}$ and $b_{\text{NaI}} = 2.1 \text{ km s}^{-1}$.

The obtained Doppler widths are mostly smaller than the instrumental resolution of the UVES data. As discussed in Sect. 2.1 the Voigt profile fitting software FITLYMAN applies a de-convolution technique to remove instrumental broadening. Since the spectra are fully Nyquist sampled, i.e. $\Delta v < \delta v/2$, even the narrowest lines are well sampled (after broadening). The uncertainty of the b -values is of course higher for very small values. Furthermore, de-convolution provides only an estimate of the true widths, if the absorption was caused by a single component.

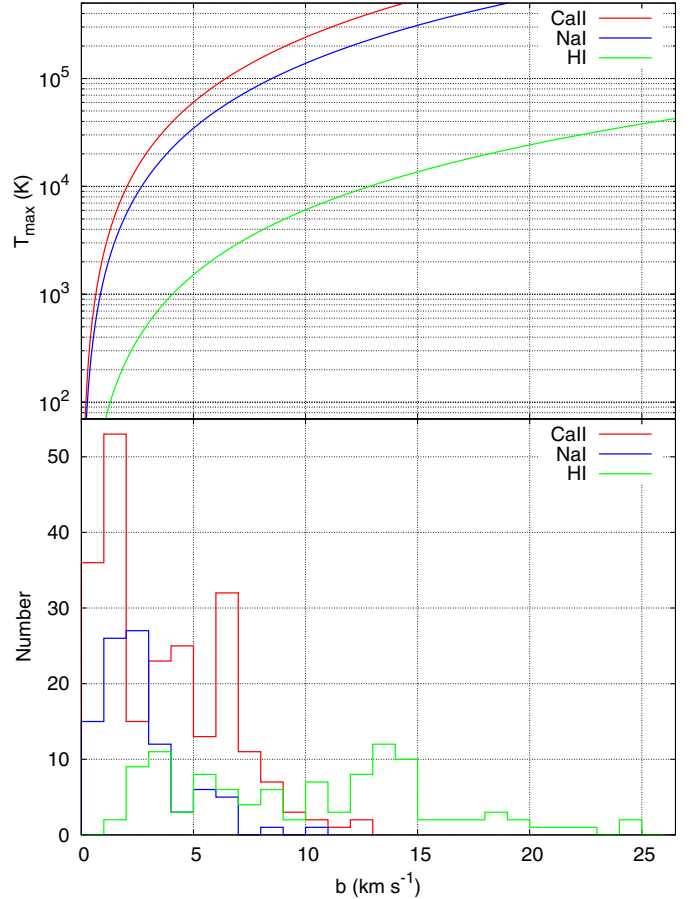


Fig. 14. Lower panel: number of Ca II, Na I and HI detections versus Doppler-parameter (b -value). Median values for the Doppler parameter are $b = 3.3 \text{ km}^{-1}$ for Ca II and $b = 2.1 \text{ km}^{-1}$ for Na I. For neutral atomic hydrogen the b -values have an enormous spread, which can most likely be explained with substructure since the spatial resolution of the 21-cm data is very coarse. For convenience we show in the upper panel the equivalent maximal (kinetic) temperatures associated with the b -values.

From the Doppler-widths one can infer an upper temperature limit, T_{max} , assuming purely thermal line-broadening, since for an ion with atomic weight A the thermal component of the b value is $b_{\text{therm}} = 0.129 (T/A)^{0.5}$. However, non-thermal broadening (e.g., by turbulence, gas flows, or unresolved velocity substructure) often contributes substantially to the observed b values in interstellar absorbers so that $b^2 = b_{\text{therm}}^2 + b_{\text{non-therm}}^2$ (and $T \ll T_{\text{max}}$).

For convenience we display in the top panel of Fig. 14 the T_{max} values as a function of b . Apparently, at least half of our Ca II and HI lines and about a third of the Na I lines have values for T_{max} above 10^4 K , which is unrealistically high for neutral gas traced by Ca II and Na I. This strongly hints at the presence of unresolved substructure or other broadening effects adding to the line widths. In case of HI this is not surprising given the rather low spatial resolution which can easily lead to beam-smearing. For a few sight lines this is confirmed by our previous high-resolution observations using the VLA and the WSRT where we detected small ($\varphi \lesssim 3'$) and cold ($100 \leq T_{\text{max}} \leq 4000 \text{ K}$) clumps ([Richter et al. 2005](#); [Ben Bekhti et al. 2009](#)). In addition, ultraviolet measurements of molecular hydrogen in Galactic extraplanar clouds have shown that small, dense gaseous clumps at sub-pc scale are widespread in the lower halo, in particular in intermediate-velocity clouds ([Richter et al. 1999, 2003a,b](#)).

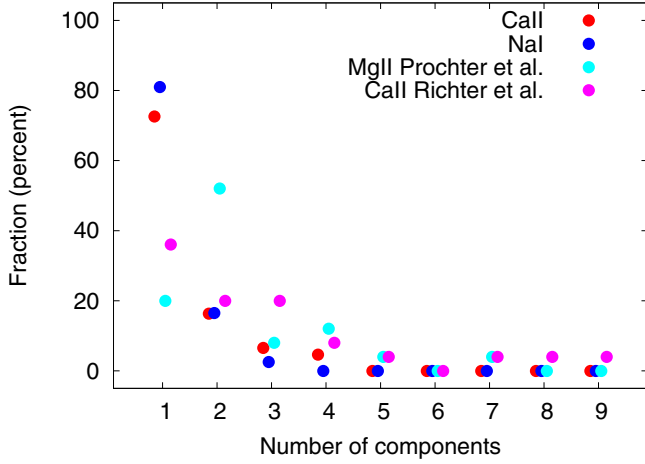


Fig. 15. Number of Ca II and Na I velocity components per absorption system. The total number of sight lines that show Ca II (Na I) absorption lines is 126 (75), but as some sight lines contain more than one independent system, we normalise with the number of independent systems (153 and 79, respectively). Furthermore, we show the results obtained by Prochter et al. (2006) and Richter et al. (2011) for comparison. Their total number of sight lines is 25 and 23, respectively.

3.3.1. Absorption component multiplicity

A fraction of the halo Ca II and Na I absorbers are composed of several velocity components. To compare our sample with other studies we show in Fig. 15 the number of velocity components per absorber (normalised to the total number of absorbers in our sample). Most of our systems show a single absorption component, about 20% are found in double-component systems, while systems with more than two components are rare in our sample. This is different from the samples studied by Prochter et al. (2006) and Richter et al. (2011), which both exhibit higher component multiplicity. This is not surprising, however, as these surveys also sample gas discs which have, together with the surrounding halo gas, a more complex velocity structure compared to halo absorbers alone.

The median group width (of systems with ≥ 2 lines) is 14 km s^{-1} for Ca II and 15 km s^{-1} for Na I. The small separation in velocity indicates that the multiple (mostly two) components are usually part of a gas structure being physically connected.

3.4. Equivalent widths

The distribution of the Ca II and Na I equivalent widths W_λ for the stronger transitions $\lambda 3934$ and $\lambda 5892$ are shown in Fig. 16. In our sample the majority of Ca II equivalent widths is below $W_\lambda^{\text{Ca II}} \lesssim 150 \text{ m}\text{\AA}$ and for Na I we find $W_\lambda^{\text{Na I}} \lesssim 250 \text{ m}\text{\AA}$. If we use $W_\lambda = 300 \text{ km s}^{-1}$ as a separation between weak and strong absorption systems (e.g., Richter et al. 2011), we find that our sample contains almost exclusively weak systems (note that most of these systems would not be observable with low spectral resolution). Furthermore, the equivalent widths are smaller than in the extra galactic sample of Richter et al. (2011). Again, this is probably due to the fact that we do not trace discs in our absorption line sample.

3.5. Area filling factors

To estimate the area filling factor of the Ca II/Na I-absorbing gas in the halo we compute the fraction of sight lines that show

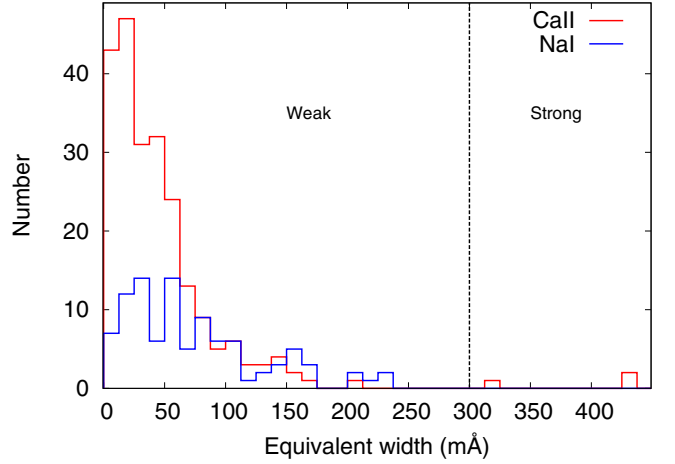


Fig. 16. Number of Ca II and Na I absorption systems versus their equivalent width. The dashed line represents the equivalent width of $W_\lambda = 300 \text{ km s}^{-1}$, which separates weak from strong absorption systems according to Mg II systems.

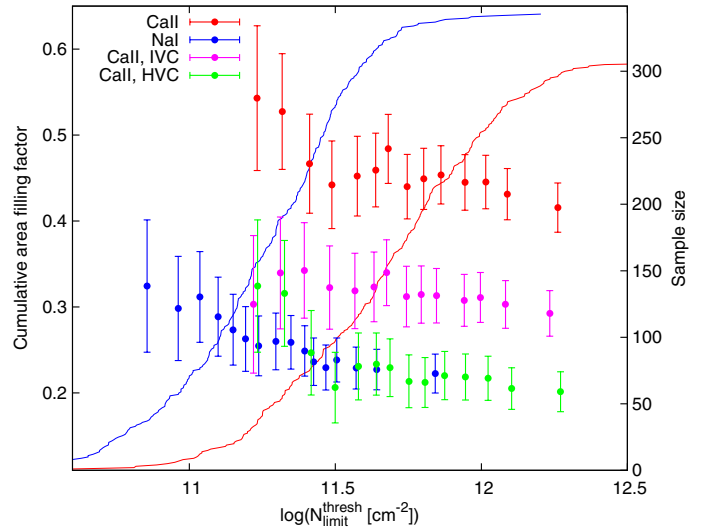


Fig. 17. Cumulative area filling factors, computed by applying column density thresholds to our sample, i.e., using only those spectra whose (theoretical) column density detection limits are below the threshold, $N_{\text{limit}} \leq N_{\text{limit}}^{\text{thresh}}$. The solid curves show the size of the sub-samples with increasing threshold.

Ca II/Na I absorption with respect to the total number of observed sight lines. This gives a total Ca II (Na I) filling factor of about 40% (25%). For high-velocity absorbers, the total Ca II (Na I) filling factors are about 20% (2%), while for intermediate velocities we find 30% (20%).

However, as we have seen earlier, the nominal detection limits vary substantially for the different sight lines. To account for that effect we show in Fig. 17 cumulative area filling factors. These were calculated by applying N_{limit} thresholds (using all spectra for which $N_{\text{limit}} \leq N_{\text{limit}}^{\text{thresh}}$) to the sample, i.e., the left-most values result from the smallest sub-sample but having the lowest noise in the spectra. The sub-sample grows in size with increasing threshold levels but the mean spectral quality decreases. The right-most values reflect the area filling factor of the full sample.

Not surprisingly, the area filling factor is notably higher for lower $N_{\text{limit}}^{\text{thresh}}$. If one only takes into account the highest-quality spectra, which allow for the detection of absorbers with $\log(N_{\text{CaII}}/\text{cm}^{-2}) \geq 11.4$ ($\log(N_{\text{NaI}}/\text{cm}^{-2}) \geq 10.9$), the area filling factor is as high as 50% (35%). Such an effect was also seen by Wakker (1991) who applied different brightness temperature thresholds to HI emission data obtained from an HVC survey. Wakker (2004) reported on typical HI area filling factors for HVCs, of order 15% for $N_{\text{HI}} > 2 \times 10^{18} \text{ cm}^{-2}$, and increasing to 30% for $N_{\text{HI}} > 7 \times 10^{17} \text{ cm}^{-2}$.

We have obtained a sufficient number of Ca II detections to also compute the cumulative area filling factors of HVCs and IVCs separately (see Fig. 17 green and purple points). There might be an increase of the HVC filling factor below $\log(N_{\text{limit}}^{\text{thresh}}/\text{cm}^{-2}) \lesssim 11.4$ but more data would be needed to obtain a statistically significant detection.

3.6. Possible association with known IVC or HVC complexes

A total of 102 Ca II (45%) and 38 Na I (40%) components in our sample is possibly associated with known IVC or HVC complexes; see Table 1. Due to the unknown distances of the absorption systems (and many complexes) the only indicator for an association can be the position and velocity of each absorber. We also analysed how many groups of lines are associated. The latter number yields a more reasonable estimate of the correlation with complexes, as a single complex could produce several absorption lines. Also, a simple counting of sight lines containing an IVC/HVC association would completely neglect the possibility of having several groups in a single sight line, some of them eventually associated with a complex, while others are not. In total, we have 138 IVC and 66 HVC groups in our sample, with 83 and 38 groups being associated with known complexes, respectively. This in turn means that there is a substantial fraction of low-column density absorption systems that possibly do not belong to a known HVC/IVC complex.

To study whether there is a fundamental difference in the properties of the components that belong to a complex and those that do not (i.e., “field” absorbers), we show in Fig. 18 column density histograms of these two populations. We find no significant difference with respect to the shape of the distributions, except that for HVC Ca II components several of the associated detections have column densities below $\log(N_{\text{CaII}}/\text{cm}^{-2}) \approx 11$. This is not observed for “field” components. However, number counts are rather low in this column density regime. When looking at the HI emission associated with the absorption, we do not detect any of the “field” HVC components. For the components that are associated with an HVC complex about 25% show HI. For intermediate-velocity features we see no significant deviation from the overall fraction $p(\text{HI}|\text{CaII})$ and $p(\text{HI}|\text{NaI})$, respectively.

The majority of the absorbers (30 IVCs and 35 HVCs) is associated with the Magellanic System (MS). In a few cases it is not clear whether they should be attributed to the MS or the anti-center shell (AC-shell), which have intermediate velocities. For 11 of the HVC and 17 of the IVC groups we have corresponding HI detections. Two sight lines (HE 0251–5550 and PKS 0506–61) are possibly associated with the Large Magellanic Cloud (LMC). From the ten absorption components with the highest deviation velocities of $|v_{\text{dev}}| > 250 \text{ km}^{-1}$ in our sample, seven are likely associated with the Magellanic System (the corresponding HI data show no emission lines). The remaining three components cannot be associated with a complex.

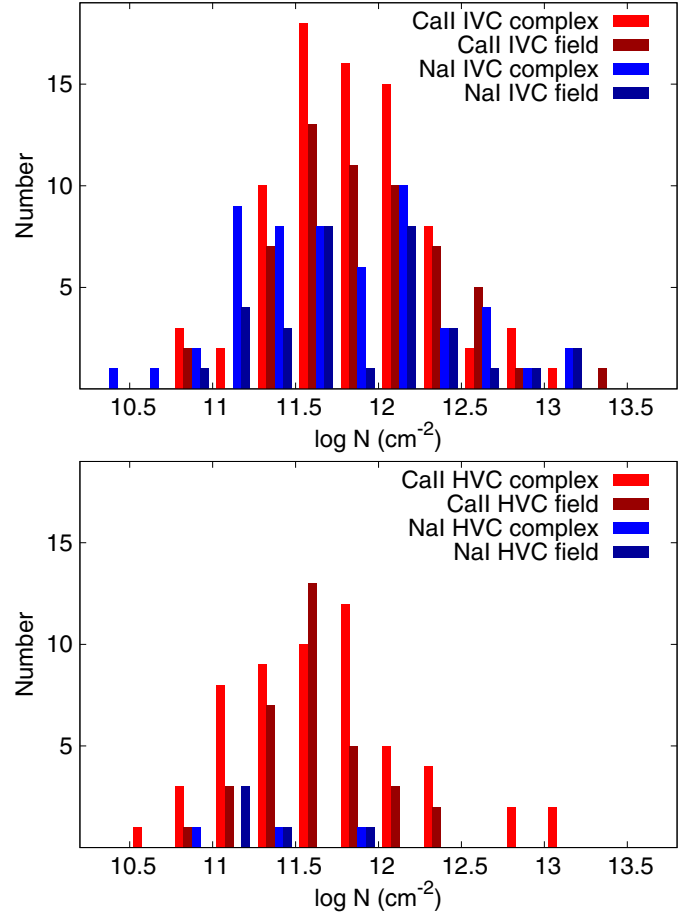


Fig. 18. Column density histograms for components (not) associated to an IVC/HVC complex.

The directions towards QSO B1448–232 and PKS 1508–05 indicate a possible association with the HVC complex L. While for QSO B1448–232 the LSR velocities are in agreement with the velocity range observed for complex L ($v_{\text{lsr}} = -188 \dots -91 \text{ km s}^{-1}$ Wakker 2004), the absorption system in the direction of PKS 1508–05 shows low negative velocities $v_{\text{lsr}} \approx -17 \dots -43 \text{ km s}^{-1}$. Such an intermediate-velocity part has not been observed previously in complex L. Eight intermediate- and two high-velocity groups are likely associated with the AC-shell, nine with complex GCN, and two with Galactic center positive (GCP).

17 IVC groups are associated with the intermediate-velocity Spur (IV-Spur). For 11 of these groups we have HI data showing corresponding emission in 10 cases. The sight-line without HI emission (3C 281) passes the outer (clumpy) region of the IV-Spur.

The intermediate-velocity complex PP-Arch hosts six of our absorption structures. Seven are related to the intermediate-velocity Arch (IV Arch), though in the case of TON 1480 the absorption component has a rather high deviation velocity of $v_{\text{dev}} = -75 \text{ km s}^{-1}$. Therefore, it is not entirely clear whether the latter is really part of the IV Arch. Two components in the direction of PKS 1629+120 are possibly related to the IVC complex K and one absorption component in the direction of SDSS J014631.99+133506.3 is associated with the IVC complex ACHV. The sight lines towards seven QSOs pass the HVC complex WA and three pass complex WD. However, the absorption components are located at intermediate velocities.

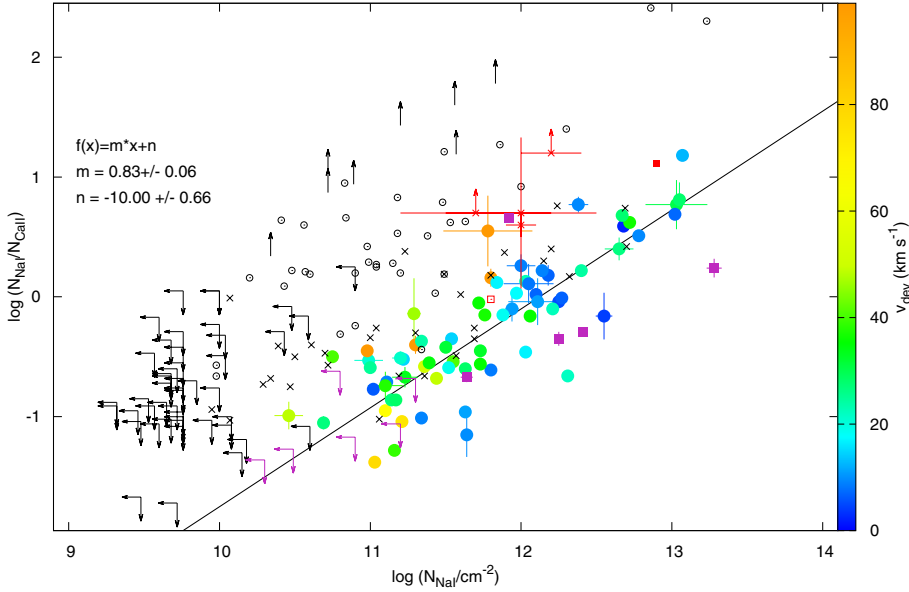


Fig. 19. Na I/Ca II ratios as a function of $\log N_{\text{NaI}}$. The red symbols show the DLA data ($1.06 \leq z \leq 1.18$) of Kondo et al. (2006, see their Fig. 5 for a detailed explanation of the different symbols). Black circles and crosses show the data for the Ca II and Na I absorbers in Milky Way (Vallerga et al. 1993) and in the LMC (Vladilo et al. 1993), respectively. Purple symbols show higher-redshift absorption lines extracted from our sample (Richter et al. 2011). Filled circles show the ratios found in our MW halo sample, with deviation velocities colour-coded. The black solid line represents a power-law fit with slope $\beta = 0.8 \pm 0.1$.

3.7. The Na I/Ca II ratio and dust depletion

As discussed earlier, the determination of absolute calcium and sodium abundances in the absorbers is afflicted with large systematic uncertainties related to the unknown amount of calcium/sodium being depleted onto dust grains, to beam smearing and to ionisation effects.

To study the degree of dust depletion in the absorbers, the $N_{\text{NaI}}/N_{\text{CaII}}$ ratio has often been used as a probe (Welsh et al. 1990; Bertin et al. 1993; Crawford et al. 2002; Kondo et al. 2006), because sodium is hardly depleted onto grains while calcium can be strongly depleted (Savage & Sembach 1996).

Values of $N_{\text{NaI}}/N_{\text{CaII}} \leq 20$ are expected in diffuse, warm ($T \approx 10^3$ K), low-density ($n_{\text{H}} \approx 10 \text{ cm}^{-3}$) neutral and partly ionised gas, where much of the calcium remains in the gas phase (Crawford et al. 2002). In contrast, values of $N_{\text{NaI}}/N_{\text{CaII}} \geq 100$ are expected in cold ($T \approx 30$ K), dense ($n_{\text{H}} \geq 10^3 \text{ cm}^{-3}$) interstellar regions.

To compare the derived $N_{\text{NaI}}/N_{\text{CaII}}$ ratios for the halo absorbers with absorbers located in different environments we display in Fig. 19 column density ratios as a function of $\log N_{\text{NaI}}$. Three other data sets were kindly provided by Sohei Kondo (see also Kondo et al. 2006). The red symbols show damped Lyman α (DLA) data ($1.06 \leq z \leq 1.18$) obtained by Kondo et al. (2006) with the near-infrared instrument IRCS (Infrared Camera and Spectrograph) installed at the Subaru Telescope. Black circles show the data for the Milky Way by Vallerga et al. (1993) who observed Ca II and Na I absorbers towards 46 early type stars in the local ISM with distances between $d = 20 \dots 500$ pc with the Coudé Echelle Spectrograph (CES) installed at the 3-m Shane telescope (Lick Observatory). Black crosses are values obtained for the LMC (Vladilo et al. 1993). For the latter the CES instrument was used to observe Ca II and Na I absorbers towards 16 stars in a $30' \times 30'$ region of the LMC centred on SN 1987A. Purple symbols show higher-redshift absorption lines extracted from our sample (see Richter et al. 2011). The filled circles represent our $N_{\text{NaI}}/N_{\text{CaII}}$ ratios, with colour-coded deviation velocities. The black solid line represents a power-law fit of the form

$$\log(N_{\text{NaI}}/N_{\text{CaII}}) = (0.8 \pm 0.1) \cdot \log(N_{\text{NaI}}/\text{cm}^{-2}) + (-10 \pm 1) \quad (11)$$

through our data.

We find that the $N_{\text{NaI}}/N_{\text{CaII}}$ ratios in our sample are systematically smaller than those in the DLAs, in the LMC and in the Milky Way. This is not surprising since the halo absorbers are expected to contain less dust than gas clouds located in the discs of galaxies. Furthermore, apart from the dependency of the ratios on $\log N_{\text{NaI}}$, there is a trend with deviation velocities. While low-velocity clouds reside mainly in the higher-column density regime, clouds with higher velocities are located in the lower left of the figure. This indicates that high-velocity clouds in our sample have less depletion of Ca II onto dust simply because the HVCs contain much less dust. The dust content gets larger with higher column densities such that the Na I/Ca II ratio increases again. This trend is known as the ‘‘Routly-Spitzer’’ effect (Routly & Spitzer 1952).

3.8. Ca II and Na I abundances

We detect H I emission for many absorption components so that we can statistically investigate the Ca II/H I and Na I/H I ratios (see Fig. 20). For completeness we show the relation found by Wakker & Mathis (2000, dashed line) along a best linear fit of our data (solid line), but note that the numbers are affected by systematic effects like beam-smearing or beam-filling and should be treated with caution. Beam-smearing is due to the finite angular resolution of the single-dish observations, which can lead to either over- or underestimation of the true H I content along the QSO sight lines³. It is difficult to estimate the exact strength of both effects (which work against each other), even statistically, since the true angular and size distribution at small scales is not well-known. Previous studies with radio-synthesis telescopes (Richter et al. 2005; Ben Bekhti et al. 2009) have shown that the H I features associated with the halo absorption systems are very clumpy on scales below $1'$ to $3'$. Unfortunately, it turned out to be difficult to find a system where an H I clump is exactly aligned with a QSO sight line, which would be required

³ Overestimation (beam-smearing problem) is due to a strong source of emission right next, i.e. within a beam size, to the QSO line of sight (but not much H I being exactly on the sight line), while underestimation (beam-filling problem) is caused if an H I feature is aligned with the QSO, but is much smaller than the single-dish beam.

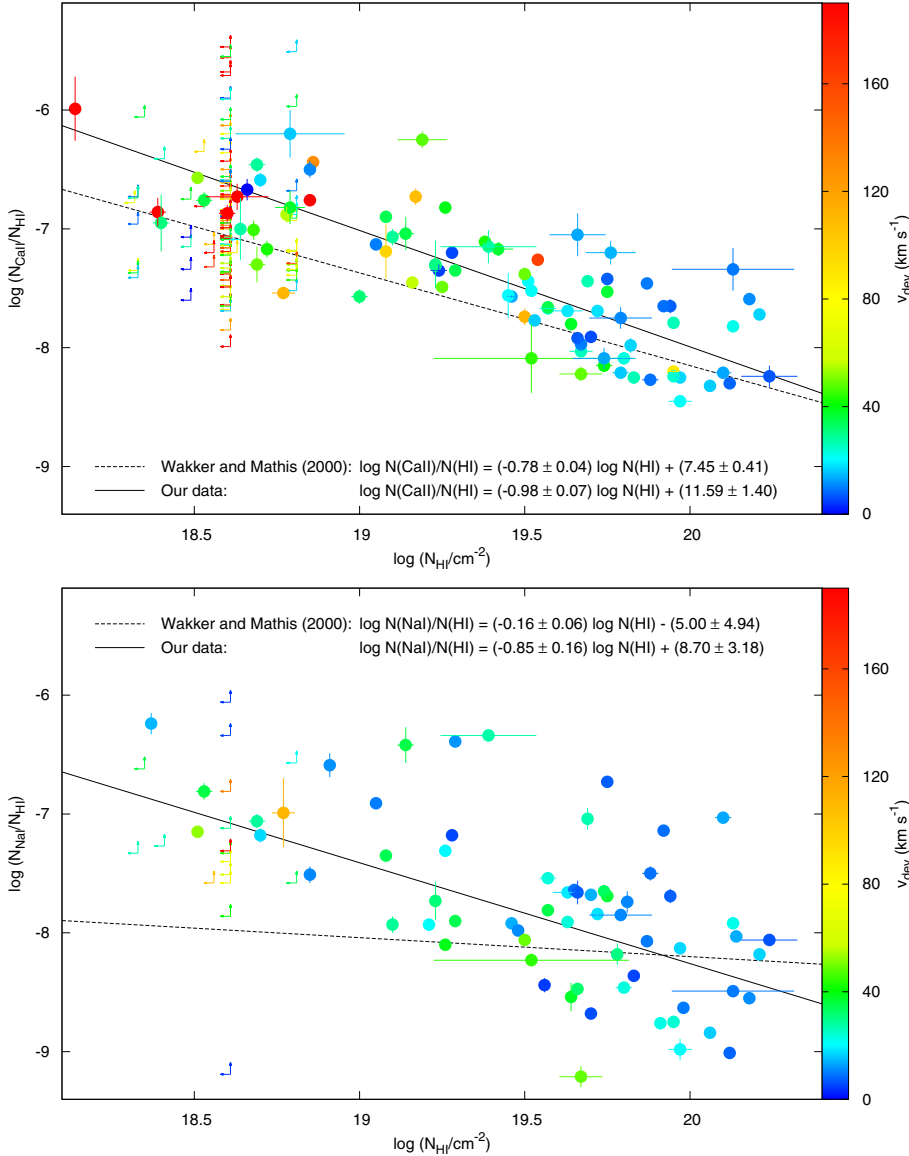


Fig. 20. Ca II/H I and Na I/H I ratios calculated for our sample. Arrows show lower limits (associated with H I non-detections). The colour of the data points marks their deviation velocity. The solid black line shows the best linear fit to the data, for comparison we have also plotted the relations found by [Wakker & Mathis \(2000\)](#), dashed line).

to have a sufficiently solid estimate of the local Ca II/H I and Na I/H I ratios.

Nevertheless, Fig. 20 allows us at least to study some statistical trends. Arrows indicate lower limits of the Ca II/H I and Na I/H I ratios (from the non-detection of hydrogen). The colour of the data points indicates their deviation velocity. Most of the higher-velocity absorbers have not been detected in H I. The colour coding shows that the non-detections are mostly high-velocity absorbers; many of these obviously have low H I column densities and/or small angular sizes so that they are not detected in H I 21-cm emission.

Figure 20 reveals similar trends for Ca II and Na I (the ion ratios decrease with increasing H I column densities). One important difference is that Ca II absorbers with higher radial velocities have generally higher Ca II/H I ratios, while for Na I such a trend is not as clearly visible. This indicates that the high-velocity absorbers have a lower dust content (i.e., less calcium depletion and higher Ca II/H I ratio) than low-velocity systems. Note that the solar abundance of Ca II/H I is about -5.7 ([Anders & Grevesse 1989](#)).

3.9. Comparison with Ca II and Mg II absorption systems at redshifts $z > 0$

Our data shows that the Milky Way halo hosts a large number of low-column density Ca II and Na I absorbers at intermediate- and high-velocities. If the Milky Way is a typical spiral galaxy in the local Universe one would expect to find similar absorption systems around other low-redshift galaxies. Therefore, [Richter et al. \(2011\)](#) used 304 QSO spectra from the same UVES data set to search for Ca II absorbers at redshifts of $z \lesssim 0.5$. They found 23 intervening Ca II absorbers, some of which have physical properties similar to those of the Milky Way halo structures. The detected column densities are in the range of $\log(N_{\text{CaII}}/\text{cm}^{-2}) = 11.25 \dots 13.04$, where the absorbers with $\log(N_{\text{CaII}}/\text{cm}^{-2}) > 11.5$ trace neutral and mildly ionised gas with $\log(N_{\text{HI}}/\text{cm}^{-2}) > 17.5$. One important result is that intervening Ca II absorbers outnumber damped Ly- α systems at low redshift by a factor of three, indicating that most of these systems trace low-column density gas in the outskirts of galaxies (i.e. they represent IVC/HVC analogues).

A good tracer for extra-planar gaseous structures around galaxies at higher redshifts is the Mg II doublet. There are two different populations of Mg II absorbers, the weak and the strong Mg II ones. While weak Mg II absorbers are thought to be located in the distant outskirts of galaxies, the strong Mg II systems are most likely located in the inner halo or even in the discs of galaxies (e.g., Petitjean & Bergeron 1990; Charlton & Churchill 1998; Churchill et al. 1999; Ding et al. 2003b). A certain fraction of strong Mg II absorbers therefore is expected to represent the analogues of IVCs/HVCs. In the MW halo several Mg II absorbers could be associated with known IVC/HVC complexes (e.g., Savage et al. 2000).

We can now compare our CDD functions with the results of Churchill et al. (2003) for Mg II and with those of Richter et al. (2011) for Ca II. In case of Ca II the power-law slope, $\beta_{\text{Ca II}} = -2.2$, is steeper than the value derived by Richter et al. (2011, $\beta_{\text{Ca II}} = -1.7$) and that obtained for Mg II, $\beta_{\text{Mg II}} = -1.59 \pm 0.05$ (Churchill et al. 2003), inferred from strong Mg II absorbers at intermediate redshifts ($z = 0.4-1.2$). As discussed in Sect. 3.1.1, this can be explained with the different absorber environments (disc+halo vs. halo) and the different dust-depletion levels.

3.10. Small-scale structure

Since our QSO sample has a random sky distribution it is not very well-suited to study small-scale structure in Milky Way halo gas. Nevertheless, a few sight lines intersect the halo with relative angular separations of less than $\sim 1^\circ$. Cross-correlating all sight lines showing halo Ca II absorption with every other sight line in our sample having at least the same S/N level (to avoid selection effects), we identify 11 of such cases. Out of these, three sightlines show absorption components matching in radial velocity. For the pair QSO J1039–2719/QSO J1040–2727 (angular separation: $17'$) at a radial velocity of $v_{\text{lsr}} = -17 \text{ km s}^{-1}$ and $v_{\text{lsr}} = -11 \text{ km s}^{-1}$, respectively, we find consistent column densities of $\log(N_{\text{Ca II}}/\text{cm}^{-2}) = 12.5$ and 12.6 . However, only the latter sight line shows also a high-velocity absorber at $v_{\text{lsr}} = 180 \text{ km s}^{-1}$. The second (very close) pair 2QZ J225153.1–314620/2QZ J225154.8–314521 (angular distance: $1'$) has a match at $v_{\text{lsr}} = -32 \text{ km s}^{-1}$, but again (in the latter sight line) two components remain undetected. Finally, in the third case, even four sight lines are close to each other (2QZ J232046.7–294406, 2QZ J232114.2–294725, 2QZ J232059.3–295521, and 2QZ J232121.2–294351; angular distance: $\leq 10'$). However, only the first two QSOs reveal one matching absorption component at $v_{\text{lsr}} = -49 \text{ km s}^{-1}$, which varies by 0.5 dex in column density, i.e. $\log(N_{\text{Ca II}}/\text{cm}^{-2}) = 12.9$ vs. 12.4 . Two IVC features in 2QZ J232046.7–294406 and an HVC in 2QZ J232114.2–294725 remain undetected in the other sight lines as well.

For all of the eight other pairs, the halo absorption components detected in one spectrum have no counterparts in the other (within a radial velocity of $\leq 50 \text{ km s}^{-1}$).

The situation is similar for Na I. Seven pairs were found, four of them show one component (each) in one spectrum with a matching absorption line in the other spectrum, but only two of these four also have similar column densities. For all remaining components/pairs, column density variations of at least ~ 0.5 dex (or non-detection in one of the sight lines) occurs.

Although the total number of pairs is small, the few examples listed above suggest that the halo structures traced by Ca II and Na I must be variable on angular scales of less than a fraction of a degree. This result is consistent with previous high-resolution radio observations (Richter et al. 2005; Ben Bekhti et al. 2009).

4. Summary

With this study we have continued our project to systematically analyse the absorption properties of neutral gas in the Milky Way halo. We present results for a significantly enlarged data sample of 408 extragalactic sight lines through the Milky Way halo. Optical QSO spectra observed with VLT/UVES were combined with data from the new EBHIS and GASS surveys to search for Ca II and Na I absorption and corresponding HI emission features of neutral gas structures in the Milky Way halo.

The main results can be summarised as follows:

1. The filling factor (or covering fraction) of Ca II/Na I absorbing gas in the halo is substantial. We detect Ca II/Na I halo absorption in about 40%/25% of all sight lines. If one corrects for selection effects by applying (column-density) thresholds, the filling factors further increase by 10%. Our large sample size allows us to separately study intermediate- and high-velocity absorbers (IVCs and HVCs).
2. Associated HI 21-cm emission is found for 50% of all Ca II halo absorption components and for nearly all Na I lines. These numbers reflect our HI 21-cm detection limits for the absorbing halo structures. While the Na I and HI data probe a similar HI column density regime down to few 10^{18} cm^{-2} , Ca II absorption arises also in gas at lower HI column densities.
3. About half of all halo absorption components appear to be associated with known IVC and HVC complexes. Interestingly, for none of the high-velocity “field” components (i.e., halo absorbers that are not connected to a known HVC complex) HI emission was detected, while for the halo absorbers related to known HVCs about 25% have HI counterparts. For IVCs such a phenomenon is not observed.
4. The observed Ca II and Na I column density distribution functions follow a power-law $f(N) = CN^\beta$, with slopes $\beta_{\text{Ca II}} = -2.2 \pm 0.2$ and $\beta_{\text{Na I}} = -1.4 \pm 0.1$. The former is steeper than what is found in extra-galactic absorber samples, which may be explained by the different absorber environments (disc vs. halo) and dust-depletion effects. Using the correlation between Ca II, Na I and HI we can convert the column densities to HI column densities. It turns out that the (converted) distributions ($\beta_{\text{HI}[\text{Ca II}]} = -1.26 \pm 0.02$ and $\beta_{\text{HI}[\text{Na I}]} = -1.44 \pm 0.06$) are roughly consistent with slopes derived for Galactic IVCs/HVCs based on HI 21-cm surveys.
5. The $N_{\text{Na I}}/N_{\text{Ca II}}$ ratios in the halo absorbers, that can be used as a probe for the dust content in the gas are systematically smaller than those in DLAs, in the LMC, and in the Milky Way disc. As expected, depletion of Ca II onto dust grains is less important in the high-velocity absorbers, where metallicities and densities are expected to be lower than in gas close to the disc.
6. Most of the Ca II and Na I absorbers show single- or double-component absorption, with b -values of $< 7 \text{ km s}^{-1}$. Nevertheless, b -values are generally too high to be purely thermal, suggesting that other broadening mechanisms (unresolved subcomponent structure, turbulence, macroscopic gas motions) contribute to observed line widths.

Acknowledgements. The authors thank the Deutsche Forschungsgemeinschaft (DFG) for financial support under the research grant KE757/9-1 and KE757/7-1. M.T.M. thanks the Australian Research Council for a QEII Research Fellowship (DP0877998). The work is based on observations with the 100-m telescope of the MPIfR (Max-Planck-Institut für Radioastronomie) at Effelsberg. We thank Sohei Kondo for providing the data sets used in Fig. 19. We are also grateful to the referee, Bart Wakker, for many useful comments and his suggestions to improve our manuscript.

References

- Anders, E., & Grevesse, N. 1989, *Geochim. Cosmochim. Acta*, 53, 197
- Ben Bekhti, N., Richter, P., Westmeier, T., & Murphy, M. T. 2008, *A&A*, 487, 583
- Ben Bekhti, N., Richter, P., Winkel, B., Kenn, F., & Westmeier, T. 2009, *A&A*, 503, 483
- Bertin, P., Lallement, R., Ferlet, R., & Vidal-Madjar, A. 1993, *A&A*, 278, 549
- Blitz, L., Spergel, D. N., Teuben, P. J., Hartmann, D., & Burton, W. B. 1999, *ApJ*, 514, 818
- Boomsma, R., Oosterloo, T. A., Fraternali, F., van der Hulst, J. M., & Sancisi, R. 2008, *A&A*, 490, 555
- Bouché, N., Murphy, M. T., Péroux, C., Csabai, I., & Wild, V. 2006, *MNRAS*, 371, 495
- Bouché, N., Murphy, M. T., Péroux, C., et al. 2012, *MNRAS*, 419, 2
- Brüns, C., Kerp, J., Staveley-Smith, L., et al. 2005, *A&A*, 432, 45
- Braun, R., & Burton, W. B. 1999, *A&A*, 341, 437
- Charlton, J. C., & Churchill, C. W. 1998, *ApJ*, 499, 181
- Charlton, J. C., Churchill, C. W., & Rigby, J. R. 2000, *ApJ*, 544, 702
- Churchill, C. W., Rigby, J. R., Charlton, J. C., & Vogt, S. S. 1999, *ApJS*, 120, 51
- Churchill, C. W., Vogt, S. S., & Charlton, J. C. 2003, *AJ*, 125, 98
- Crawford, I. A., Lallement, R., Price, R. J., et al. 2002, *MNRAS*, 337, 720
- de Boer, K. S. 2004, in *High Velocity Clouds*, ed. H. van Woerden, B. P. Wakker, U. J. Schwarz, & K. S. de Boer, *Astrophys. Space Sci. Lib.*, 312, 227
- de Heij, V., Braun, R., & Burton, W. B. 2002, *A&A*, 391, 125, 98
- Dekker, H., D'Odorico, S., Kaufer, A., Delabre, B., & Kotzłowski, H. 2000, in *Optical and IR Telescope Instrumentation and Detectors*, ed. M. Iye, & A. F. Moorwood, *Proc. SPIE*, 4008, 534
- Ding, J., Charlton, J. C., Bond, N. A., Zonak, S. G., & Churchill, C. W. 2003a, *ApJ*, 587, 551
- Ding, J., Charlton, J. C., Churchill, C. W., & Palma, C. 2003b, *ApJ*, 590, 746
- Fontana, A., & Ballester, P. 1995, *The Messenger*, 80, 37
- Fox, A. J., Savage, B. D., & Wakker, B. P. 2006, *ApJS*, 165, 229
- Fraternali, F., Oosterloo, T., Sancisi, R., & van Moorsel, G. 2001, in *Gas and Galaxy Evolution*, ed. J. E. Hibbard, M. Rupen, & J. H. van Gorkom, *ASP Conf. Ser.*, 240, 286
- Fraternali, F., Oosterloo, T., Boomsma, R., Swaters, R., & Sancisi, R. 2004, in *Recycling Intergalactic and Interstellar Matter*, ed. P.-A. Duc, J. Braine, & E. Brinks, *IAU Symp.*, 217, 136
- Fraternali, F., Binney, J., Oosterloo, T., & Sancisi, R. 2007, *New Astron. Rev.*, 51, 95
- Hill, A. S., Haffner, L. M., & Reynolds, R. J. 2009, *ApJ*, 703, 1832
- Kalberla, P. M. W. 2003, *ApJ*, 588, 805
- Kalberla, P. M. W., Mebold, U., & Reich, W. 1980, *A&A*, 82, 275
- Kalberla, P. M. W., Burton, W. B., Hartmann, D., et al. 2005, *A&A*, 440, 775
- Kalberla, P. M. W., Dedes, L., Kerp, J., & Haud, U. 2007, *A&A*, 469, 511
- Kalberla, P. M. W., McClure-Griffiths, N. M., Pisano, D. J., et al. 2010, *A&A*, 521, A17
- Kaufmann, T., Mayer, L., Wadsley, J., Stadel, J., & Moore, B. 2006, *MNRAS*, 370, 1612
- Kerp, J., Burton, W. B., Egger, R., et al. 1999, *A&A*, 342, 213
- Kerp, J., Winkel, B., Ben Bekhti, N., Flöer, L., & Kalberla, P. M. W. 2011, *Astron. Nachr.*, 332, 637
- Kondo, S., Kobayashi, N., Minowa, Y., et al. 2006, *ApJ*, 643, 667
- Lockman, F. J., Murphy, E. M., Petty-Powell, S., & Urick, V. J. 2002, *ApJS*, 140, 331
- Lu, L., Savage, B. D., & Sembach, K. R. 1994, *ApJ*, 437, L119
- Majewski, S. 2004, in *Satellites and Tidal Streams*, ed. F. Prada, D. Martinez Delgado, & T. J. Mahoney, *ASP Conf. Ser.*, 327, 63
- Marasco, A., & Fraternali, F. 2011, *A&A*, 525, A134
- Masiero, J. R., Charlton, J. C., Ding, J., Churchill, C. W., & Kacprzak, G. 2005, *ApJ*, 623, 57
- McClure-Griffiths, N. M., Pisano, D. J., Calabretta, M. R., et al. 2009, *ApJS*, 181, 398
- Muller, C. A., Oort, J. H., & Raimond, E. 1963, *C. R. Acad. Sc. Paris*, 257, 1661
- Oosterloo, T., Fraternali, F., & Sancisi, R. 2007, *AJ*, 134, 1019
- Petitjean, P., & Bergeron, J. 1990, *A&A*, 231, 309
- Petitjean, P., Webb, J. K., Rauch, M., Carswell, R. F., & Lanzetta, K. 1993, *MNRAS*, 262, 499
- Prochter, G. E., Prochaska, J. X., & Burles, S. M. 2006, *ApJ*, 639, 766
- Putman, M. E., de Heij, V., Staveley-Smith, L., et al. 2002, *AJ*, 123, 873
- Putman, M. E., Staveley-Smith, L., Freeman, K. C., Gibson, B. K., & Barnes, D. G. 2003, *ApJ*, 586, 170
- Richter, P. 2006, in *Rev. Mod. Astron.* 19, ed. S. Roeser, 31
- Richter, P., de Boer, K. S., Widmann, H., et al. 1999, *Nature*, 402, 386
- Richter, P., Sembach, K. R., Wakker, B. P., & Savage, B. D. 2001a, *ApJ*, 562, L181
- Richter, P., Sembach, K. R., Wakker, B. P., et al. 2001b, *ApJ*, 559, 318
- Richter, P., Savage, B. D., Sembach, K. R., Tripp, T. M., & Jenkins, E. B. 2003a, in *The IGM/Galaxy Connection, The Distribution of Baryons at $z = 0$* , ed. J. L. Rosenberg, & M. E. Putman, *Astrophys. Space Sci. Lib.*, 281, 85
- Richter, P., Wakker, B. P., Savage, B. D., & Sembach, K. R. 2003b, *ApJ*, 586, 230
- Richter, P., Westmeier, T., & Brüns, C. 2005, *A&A*, 442, L49
- Richter, P., Charlton, J. C., Fangano, A. P. M., Bekhti, N. B., & Masiero, J. R. 2009, *ApJ*, 695, 1631
- Richter, P., Krause, F., Fechner, C., Charlton, J. C., & Murphy, M. T. 2011, *A&A*, 528, A12
- Routly, P. M., & Spitzer, Jr., L. 1952, *ApJ*, 115, 227
- Rudie, G. C., Steidel, C. C., Trainor, R. F., et al. 2012, *ApJ*, 750, 67
- Sancisi, R., Fraternali, F., Oosterloo, T., & van der Hulst, T. 2008, *A&A Rev.*, 15, 189
- Savage, B. D., & Massa, D. 1987, *ApJ*, 314, 380
- Savage, B. D., & Sembach, K. R. 1996, *ARA&A*, 34, 279
- Savage, B. D., Wakker, B., Jannuzi, B. T., et al. 2000, *ApJS*, 129, 563
- Sembach, K. R., Savage, B. D., & Massa, D. 1991, *ApJ*, 372, 81
- Sembach, K. R., Wakker, B. P., Savage, B. D., et al. 2003, *ApJS*, 146, 165
- Shapiro, P. R., & Field, G. B. 1976, *ApJ*, 205, 762
- Steidel, C. C., Erb, D. K., Shapley, A. E., et al. 2010, *ApJ*, 717, 289
- Thom, C., Putman, M. E., Gibson, B. K., et al. 2006, *ApJ*, 638, L97
- Vallerga, J. V., Vedder, P. W., Craig, N., & Welsh, B. Y. 1993, *ApJ*, 411, 729
- van Woerden, H., Schwarz, U. J., Peletier, R. F., Wakker, B. P., & Kalberla, P. M. W. 1999, *Nature*, 400, 138
- Vladilo, G., Molaro, P., Monai, S., et al. 1993, *A&A*, 274, 37
- Wakker, B. P. 1991, *A&A*, 250, 499
- Wakker, B. P. 2001, *ApJS*, 136, 463
- Wakker, B. P. 2004, in *High Velocity Clouds*, ed. H. van Woerden, B. P. Wakker, U. J. Schwarz, & K. S. de Boer, *Astrophys. Space Sci. Lib.*, 312, 25
- Wakker, B. P. 2006, *ApJS*, 163, 282
- Wakker, B. P., & Mathis, J. S. 2000, *ApJ*, 544, L107
- Wakker, B. P., Howk, J. C., Savage, B. D., et al. 1999, *Nature*, 402, 388
- Wakker, B. P., York, D. G., Howk, J. C., et al. 2007, *ApJ*, 670, L113
- Wakker, B. P., York, D. G., Wilhelm, R., et al. 2008, *ApJ*, 672, 298
- Welsh, B. Y., Vedder, P. W., & Vallerga, J. V. 1990, *ApJ*, 358, 473
- Westmeier, T. 2007, *Ph.D. Thesis*, Rheinische Friedrich-Wilhelms-Universität Bonn
- Winkel, B., Kalberla, P. M. W., Kerp, J., & Flöer, L. 2010, *ApJS*, 188, 488
- Winkel, B., Ben Bekhti, N., Darmstädter, V., et al. 2011, *A&A*, 533, A105